Modelling the 2010 Chilean Tsunami using the H_2Ocean unstructured mesh model

Rachid Abraimi

Graduation Committee:
Prof. dr. Julie Pietrzak
Prof. dr. ir. Ramon Hanssen
Dr. Riccardo Riva
Dr. ir. Marcel Zijlema
Supervision from PUC:
Prof. (Assoc.) Rodrigo Cienfuego

Abstract

The 2010 Chile megathrust earthquake, with a magnitude of 8.8 on the Richter magnitude scale, occurred on February 27, 2010 at 06:34 UTC and initiated a devastating tsunami which severely hit the central coast of Chile. An intriguing aspect of this tsunami is the delayed arrival of a destructive wave, larger than the initial wave, at Talcahuano harbour three hours after the initial earthquake shock. The 2010 Chile tsunami has been modelled using H_2Ocean tsunami model using Moreno's, Delouis' and Vigny's earthquake solutions. Each earthquake model produces realistic tsunami wave fields and predicts the large wave which severally flooded the Bay of Concepción. Numerical simulations also show persistent sea surface oscillations for several hours. The computed surface elevations have been processed to compute the energy flux. The energy flux shows the presence and the important role of edge waves during this event. It shows that constructive wave interference of two edge waves over the submarine canyon nearby Cobquecura leads to the large wave which destroyed Talcahuano harbour.

Acknowledgements

I would like to take this opportunity to express my sincere gratitude to Julie Pietrzak, Ramon Hanssen, Riccardo Riva and Marcel Zijlema who supported me throughout the course of this MSc. graduation project. I am thankful for their invaluable constructive feedback and guidance during the project work. I also would like to express my warm thanks to Haiyan Cui for all his help and patience when I was learning how to use his numerical tsunami model.

Special thanks go to Julie Pietrzak for connecting me to the Pontificia Universidad Católica in Chile where I have carried out a part of my research. I would also like to thank Rodrigo Cienfuegos and Juan Carlos Dominguez for their hospitality and guidance during my stay in Chile.

Thank you,

Rachid Abraimi

Table of contents

List of Figures

List of Tables

1. Introduction

1.1. Context

The 2010 Chile earthquake, with a magnitude of 8.8 on the Richter magnitude scale, occurred on 27th of February 34 km off the coast (Servicio Sismológico, 2010). The subsea earthquake initiated a tsunami that caused a peaked localised run-up of approximately 29 m on a coastal bluff at Constitución (Fritz, et al., 2010). The Pacific Tsunami Warning Center (PTWC) issued warnings 5 minutes after the first shock (Fritz, et al., 2010). Due to the high traveling speed of the tsunami and the relative short distance of the epicentre from the coast the first wave hit the coast within 30 minutes. The result was that evacuations and warnings by local authorities were often not in time (Fritz, et al., 2010). The aftermath of the devastating earthquake and the resulting tsunami was the destruction of many buildings and more than 521 casualties (Yamazaki & Cheung, 2011). Despite the warning of PTWC most casualties occurred due to significant so called "resonance-induced waves" by Yamazaki and Cheung (2011) after the first tsunami wave hit the Chilean coast. It seems that the tsunami simulation used for warning purposes hasn't been ran for the required simulation time to catch the delayed waves or didn't predict this destructive wave at all.

1.2. Area of interest and background

The area of interest of the 2010 Chile earthquake is twofold. On the one hand the area of interest spans the central Chile Region where the 500 km long earthquake rupture struck (Figure 1.1), in particular the Talcahuano bay where severe flooding occurred due to persistent wave oscillations. On the other hand the area of interest spans the Pacific Ocean, with sea surface observations recorded by DART buoys as discussed in the paper by Yamazaki & Cheung (2011).

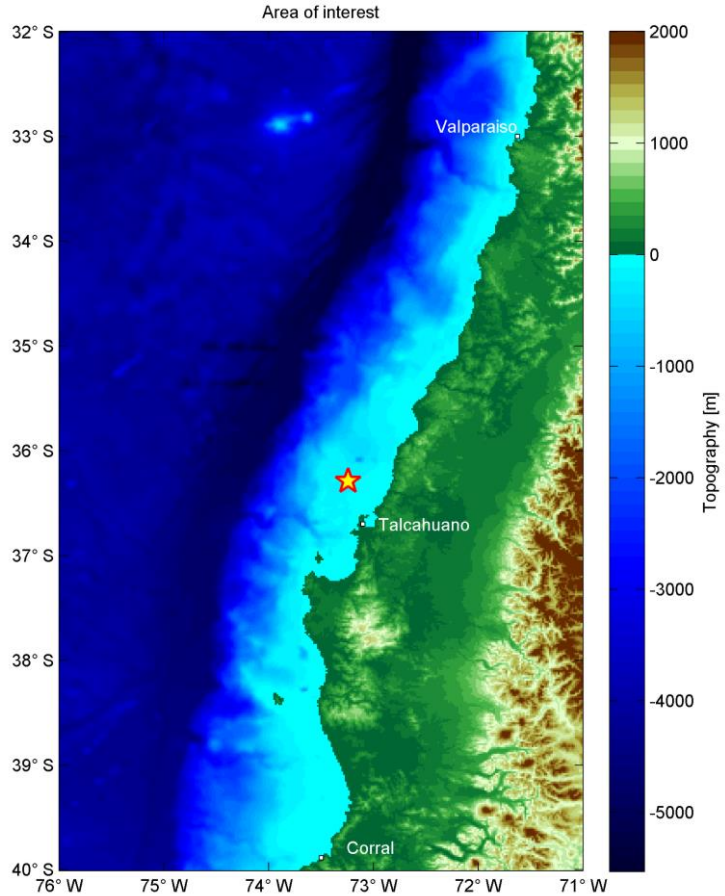

Figure 1.1: Area of interest highlighting the epicentre of the 2010 Maule earthquake (Servicio Sismológico, 2010). Valparaiso, Talcahuano and Corral are the harbours where the sea surface records are available.

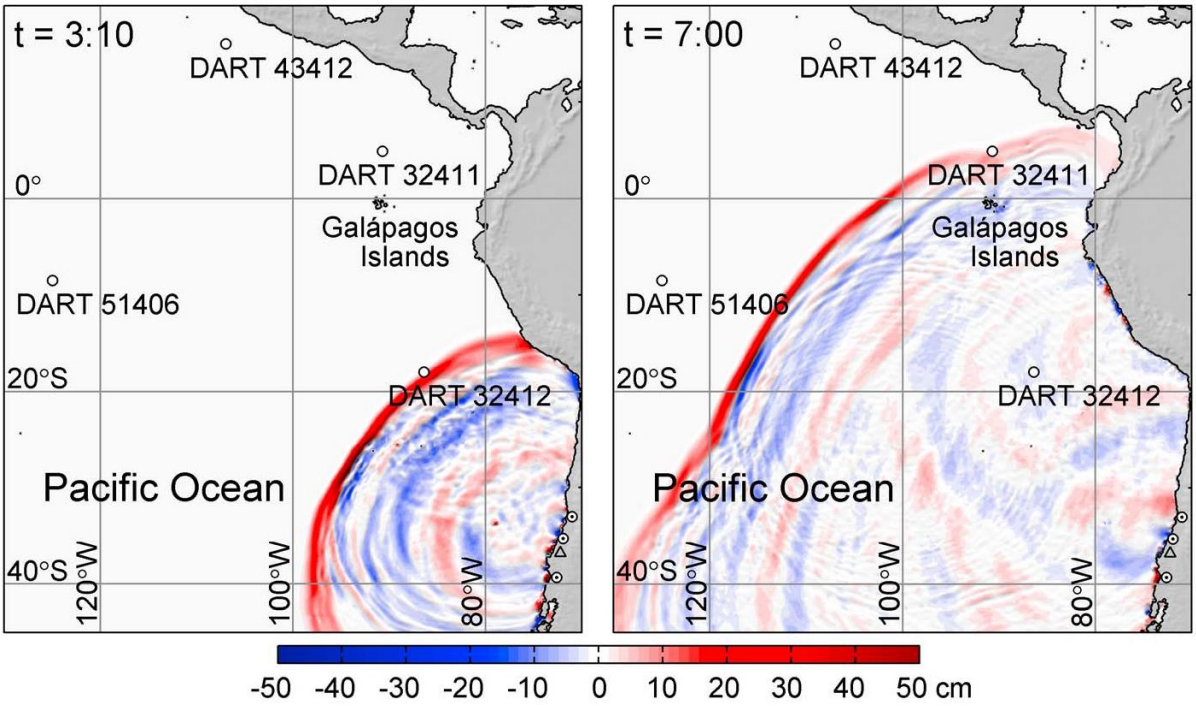

Figure 1.2: Snapshots of modelled surface elevation. Triangle indicates Talcahuano and circle-dots indicate Valparaiso, Constitución, and Tolten from north to south (Yamazaki & Cheung, 2011).

The earthquake rupture was 500 km long and 50 km wide in dimension (Yamazaki & Cheung, 2011). The resulting tsunami had a significant impact across 700 km of Chile's coast. The tide gauges show wave-amplitude of approximately 2.6 m near Valparaiso and 2.2 m at Corral, at a distance of 350 km and 420 km respectively from the epicentre. Unfortunately many tide gauges, including Talcahuano tide gauge, didn't survive this event. The International Tsunami Survey Team (ITST) reported that the tsunami wave at Talcahuano measured approximately 6 m in amplitude (Fritz, et al., 2010). This wave arrived 3 hours after the earthquake and severely flooded and damaged the bay of Concepción. The tremendous force of the tsunami at Talcahuano is highlighted in Figure 1.4. The tsunami dragged ships on land and severely damaged many buildings along the coast.

The unusual behaviour of the 2010 Chile tsunami has been investigated by Yamazaki and Cheung (2011) with the aid of NEWOWAVE, a model that solves the 2D Shallow Water Equations (SWE) (Yamazaki, Cheung, & Kowalik, 2010). They claim that the observed tsunami behaviour could be explained by shelf resonance. In the following section a short review is given on their research.

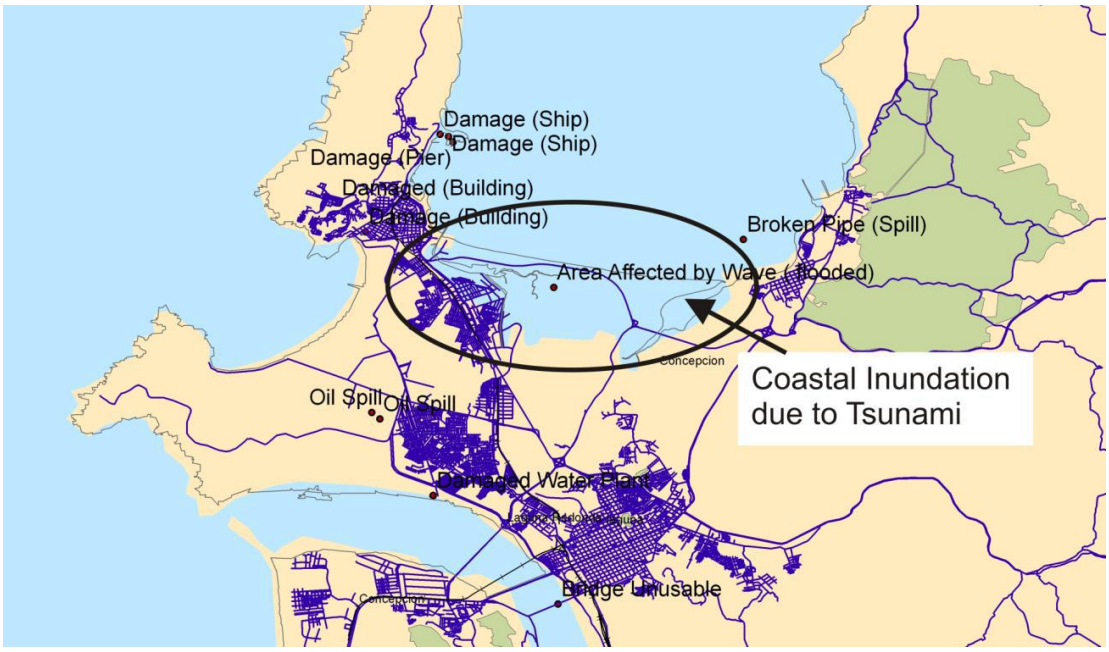

Figure 1.3: Damage map of Concepción and Talcahuano. Source: (AON Benfield, 2010).

Figure 1.4: (Top) Damaged home and fishing boat near Dichato. Bottom: Dragged and tilted ship in the Bay of Concepción (AON Benfield, 2010).

1.3. Shelf Resonance and edge waves

Simulation of the 2010 Chile tsunami carried out by Yamazaki and Cheung (2011) shows that the tsunami propagates in radial direction with a prominent initial wave over a 30° arc relative. They transformed their computed surface elevation time series by means of a Fourier transform to obtain the spectral amplitude versus frequency. They then plot the spectral amplitude of the surface elevation against the wave period. With the aid of this quantity they demonstrate the importance of the continental shelf in trapping a large portion of the wave energy. The continental slope is deemed to refract and trap the tsunami energy as progressive edge waves on the continental shelf. Depending on the angle of incidence, relative to the coast and shelf edge, of these waves, reflection between the coast and continental shelf boundaries produces a number of standing waves along the Chilean coast.

The trapped waves oscillate in the radial direction at the natural periods of the shelf and slope while the long-period waves leak into the open ocean. The process of reflection and refraction at the coast and (continental) shelf edge respectively can lead to shelf resonance if the reflected wave is in phase with a following incident wave. Shelf resonance occurs when the continental shelf is approximately $1/4, 3/4, \text{etc.}$, wave lengths wide (Webb, 1976). Yamazaki and Cheung (2011) claim that the irregular wave pattern observed during this event could be the consequence of shelf resonance. They assume that constructive interference of resonance modes caused the destruction of Talcahuano harbour.

Edge waves are a class of waves that propagate largely along the coast. Their amplitude is highest at the coast and decreases exponentially in cross-shore direction. The free surface profile in cross-shore direction and the shallow water, edge wave dispersion relation can be written in the following form (Geist, 2013):

$$\eta(x) = e^{-k_y x} L_n(2k_y x)$$
$$\left(\frac{2\pi}{T_n}\right)^2 = g k_y (2n+1)\tan(\beta) \quad (1)$$

Where n represents the edge wave mode, T_n its period, k_y the cross-shore wavenumber, β the mean ocean bottom slope and L_n the Laguerre polynomial of order n. Figure 1.5 shows the analytical solution of the free surface amplitude in the cross-shore direction for uniformly sloping bathymetry (Mei, 1983).

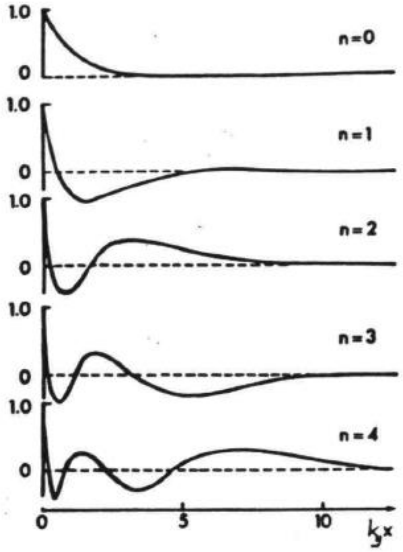

Figure 1.5: Variation of edge wave amplitude $\eta(x)$ in the cross-shore direction for modes 0,1,2,3 and 4 (Mei, 1983).

The analysis carried out by Yamazaki and Cheung (2011) provides a comprehensive understanding of the wave field observed during the Chilean tsunami. It provides to a large extent an explanation for the observed impact along the central coast of Chile and shows the natural frequency of several coastal embayment's and the role of the shelf width. A limitation of their analysis is that the conclusions are solely based on the Fourier transform of the computed surface elevation. This results in the elimination of the temporal information of the tsunami propagation which imposes a limitation when interpreting the results. It is not possible for example to prove their assumption that superposition of edge waves resulted in the destructive wave which arrived three hours later in Talcahuano. We therefore propose to use the energy flux quantity to analyse this intriguing aspect of 2010 Chile tsunami. It is expected that this quantity will give more insight in the wave propagation, particularly the evolution of edge waves which seem to dominate the wave field. The derivation, the strengths and limitations of the energy flux will be discussed Chapter 2.

1.4. Problem definition

The 2010 Chile earthquake generated a devastating tsunami which hit the Chilean coast within 30 minutes. An intriguing aspect of this event is the sustained surface oscillations for more than 4 hours after the earthquake. Normally one would expect that the amplitude after such a period would dampen out (Yamazaki & Cheung, 2011). But 3 hours after the earthquake a destructive wave, bigger than the initial earthquake-induced wave, hit the Talcahuano Harbour 100 km south of the epicentre (Larrañaga, 2010). The Chilean authority withdrew the tsunami warning before this wave arrived at Talcahuano in the bay of (Centro De Investigación Periodística, 2012). Many people returned to their homes after the withdrawal of the warning which resulted in many casualties. It seems that the advisors of the authority didn't expect delayed waves and flooding. It is therefore necessary to investigate this case further to gain comprehensive knowledge of the interaction of tsunami waves with this specific coast. Understanding of this mechanism would allow better interpretation of tsunami simulations for issuance of warnings during similar tsunami events in vulnerable coastal communities located in coastal areas which are characterised by a wide continental margin.

1.5. Research objective

The main research objective is to reach a comprehensive understanding of the persistent wave oscillations observed during the 2010 Chile tsunami. The following hypothesis is key within this research:

> *Constructive wave-interference, of an alongshore migrating edge wave with a cross-shore standing wave, is the reason for the destructive wave at Talcahuano harbour three hours after the earthquake.*

To support the hypothesis the following questions are derived:

What are the capabilities and limitations of the H_2Ocean numerical tsunami model in simulating the 2010 Chile tsunami?

What are the effects of the different earthquake scenarios (source models) on the wave field generated at Talcahuano harbour?

What is the effect of the of the Cobquecura submarine canyon on tsunami propagation?

1.6. Approach

A number of steps should be followed to verify the formulated hypothesis. First, a literature study is undertaken to gain a comprehensive understanding of the physical processes that are important for tsunamis. Subsequently, the 2010 Chile tsunami has to be simulated with H_2Ocean tsunami model. The obtained results will be compared with field observations in order to assess the H_2Ocean model setup such as the generated mesh and model parameters. Additional tsunami simulations will be carried out with the available source models which describe the vertical displacement of the earthquake rupture surface. The model-parameter setup and generated mesh will be the same for all tsunami simulations. Then the best earthquake model will be determined based on the residuals between the tsunami simulation results and the observations. The last step consists of further analysis of the tsunami model results, using the best earthquake source model, to investigate the persistent wave oscillations.

1.7. Report outline

This report is structured as follows: Chapter 2 discusses the theoretical background of tsunamis that is required to understand tsunamis in general and more in particular the generation of coastally trapped waves. The subsequent chapter explains the model setup in order to simulate the tsunami accurately. Chapter 4 explains the methods used for processing the data and model results. In Chapter 5 the simulation results will be compared to observations from tide gauges and DART buoys. Furthermore, interpretation of the simulated wave-field is given in this chapter. Finally, conclusions and recommendations based on the hypothesis and research questions are discussed in Chapter 6.

2. Theoretical background

This chapter provides a theoretical background of tsunamis. The first section briefly introduces the generation mechanism of the 2010 Chile tsunami. Subsequently the 2D shallow water equation will be derived. The succeeding section the energy flux formulation for long period waves will be derived. The focus will be on the possibilities and limitations of the energy flux method as a tool with which to analyse tsunami wave propagation wave evolution and propagation. The last section gives a qualitative description of the physics behind wave trapping.

2.1. Physics of tsunamis

2.1.1. Generation of tsunamis

Tsunamis are ocean waves usually generated by undersea landslides or earthquakes. They can travel all the way across the ocean and their amplitude increases when entering shallow waters (Vreugdenhil, 1994). In the case of Chile the earthquake occurred as a consequence of convergence of the Nazca and South American plate in the Andean subduction zone. The frequency of occurrence of a megathrust earthquake such as the 2010 Maule earthquake is one per 100-200 years in any given segment of the margin (Moreno, Rosenau, & Oncken, 2010). The oceanic Nazca plate subducts beneath the continental South America plate. During this process the South American plate abruptly rises and the coastal zone suddenly subsides. The ocean surface mimics the sea floor deformation generating a tsunami which propagates under influence of gravity in both shoreward and seaward direction (Figure 2.1). Tsunamis are characterized as shallow-water waves because of their long wavelengths. In the following section of this paragraph the derivation of the 2D shallow water equation governing the tsunami propagation will be discussed.

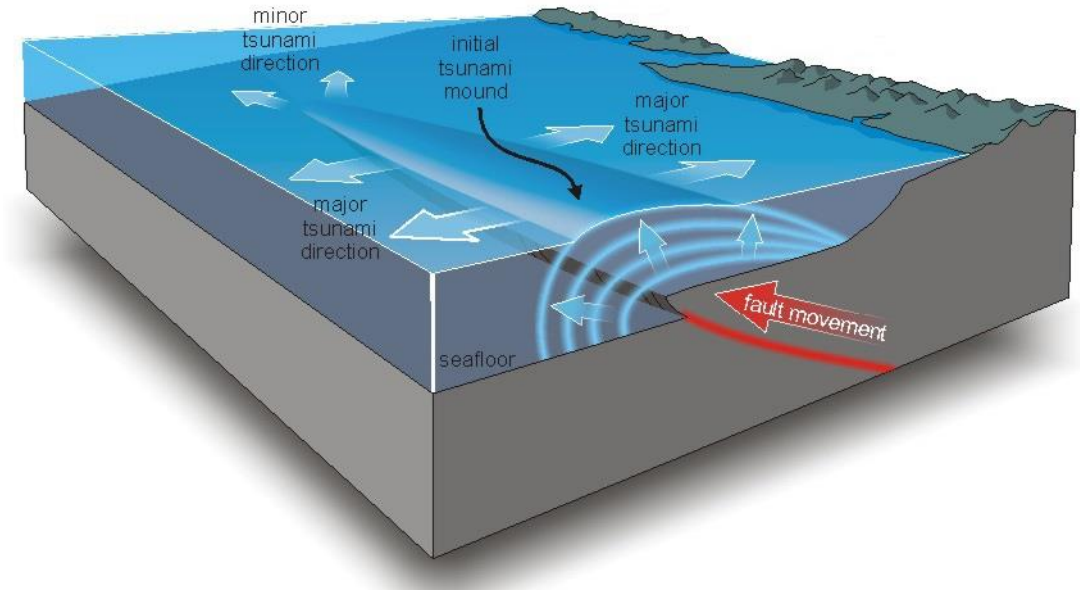

Figure 2.1: Tsunamis generated by submarine earthquakes (Richmond, 2009).

2.1.2. 2D- Shallow Water Equation

Our starting point, without deriving them, are the Reynolds Averaged Navier-Stokes equations (RANS) under the hydrostatic and Boussinesq assumptions (Pieterzak, 2013):

$$\begin{aligned}
&\frac{\partial u}{\partial t}+\frac{\partial u^2}{\partial x}+\frac{\partial uv}{\partial y}+\frac{\partial uw}{\partial z}-fv+\frac{1}{\rho_0}\frac{\partial p}{\partial x}=\frac{1}{\rho_0}\left[\frac{\partial \tau_{xx}}{\partial x}+\frac{\partial \tau_{xy}}{\partial y}+\frac{\partial \tau_{xz}}{\partial z}\right]\\
&\frac{\partial v}{\partial t}+\frac{\partial vu}{\partial x}+\frac{\partial v^2}{\partial y}+\frac{\partial vw}{\partial z}+fu+\frac{1}{\rho_0}\frac{\partial p}{\partial y}=\frac{1}{\rho_0}\left[\frac{\partial \tau_{yx}}{\partial x}+\frac{\partial \tau_{yy}}{\partial y}+\frac{\partial \tau_{yz}}{\partial z}\right]\\
&\frac{\partial p}{\partial z}=-\rho \mathrm{g}
\end{aligned} \tag{2}$$

We adopt a Cartesian co-ordinate system (x, y, z) with x positive in the East direction, y positive in the North direction and z positive upwards, (u, v, w) are the corresponding velocity components, $t,\ p,\ \rho, \rho_0$ and g represent time, pressure, density, reference density and gravitational acceleration respectively. Finally $f = 2\Omega\sin(\varphi)$ represents the Coriolis parameter which incorporates the effect of the Earth's rotation, in which Ω is the angular rate of the Earth's rotation and φ represents the geographic latitude. The stress terms on the right hand side are the Reynolds stresses, where the normal stresses are given by τ_{xx}, τ_{yy} and the shear stresses by $\tau_{xy}, \tau_{yx}, \tau_{xz}, \tau_{yz}$.

For the purpose of modelling tsunamis we can limit our attention to incompressible fluids, the continuity equation then reads:

$$\frac{\partial u}{\partial x}+\frac{\partial v}{\partial y}+\frac{\partial w}{\partial z}=0 \tag{3}$$

Please note that a incompressible fluid does not imply that the fluid density is constant, but rather means that it is independent of pressure. The density may vary due to variations in temperature and salinity. This however is not modelled in H_2Ocean and is therefore outside of the scope of this research.

In order to find a solution of the differential equations boundary conditions are needed. There are two types of boundary conditions. The kinematic boundary condition constrains the particles from crossing the free surface and the bottom boundary i.e. no normal flow:

$$\begin{aligned}
&u\frac{\partial z_b}{dx}+v\frac{\partial z_b}{dy}-w=0 \text{ at } z_b=-d\\
&\frac{\partial \eta}{dt}+u\frac{\partial \eta}{dx}+v\frac{\partial \eta}{dy}=0 \text{ at } z=\eta
\end{aligned} \tag{4}$$

Where z_b is the bottom level, measured from a horizontal reference level, see Figure 2.2. The dynamic boundary condition incorporates the forces acting at the boundary. At the bottom a no-slip condition for turbulent fluids holds. This means that the velocity at the solid boundary has to be set to zero:

$$u = v = 0 \tag{5}$$

Incorporating the bottom and surface turbulent stress yields:

$$\tau_{bx} = \tau_{xx}\frac{\partial z_b}{\partial x} + \tau_{xy}\frac{\partial z_b}{\partial y} + \tau_{xz}$$
$$\tau_{sx} = -\tau_{xx}\frac{\partial \eta}{\partial x} - \tau_{xy}\frac{\partial \eta}{\partial y} + \tau_{xz} \tag{6}$$

Where η represents the water level elevation and d the reference water depth.

The final step in deriving the 2D shallow water equation (SWE) involves the integration of the continuity equation and the horizontal momentum equation over the depth $h = -d + \eta$. Since d and η are variable in both the spatial and temporal domain integration via Leibniz rule is required. The derivation of the depth integrated continuity equation reads:

$$\begin{aligned} 0 = \int_{-d}^{\eta} \nabla \cdot \mathbf{u} &= \int_{-d}^{\eta} (\frac{\partial u}{\partial x} + \frac{\partial v}{\partial y})dz + w|_{z=\eta} - w|_{z=-d} \\ &= \frac{\partial}{\partial x}\int_{-d}^{\eta} u dz + \frac{\partial}{\partial y}\int_{-d}^{\eta} v dz - (u|_{z=\eta}\frac{\partial \eta}{\partial x} + u|_{z=-d}\frac{\partial d}{\partial x}) \\ &\quad -(\mathrm{v}|_{z=\eta}\frac{\partial \eta}{\partial y} + v|_{z=-d}\frac{\partial d}{\partial y}) + w|_{z=\eta} - w|_{z=-d} \end{aligned} \tag{7}$$

The depth-averaged velocities in the aforementioned equation equal to:

$$\bar{u} = \frac{1}{h}\int_{-d}^{\eta} u dz, \quad \bar{v} = \frac{1}{h}\int_{-d}^{\eta} v dz \tag{8}$$

Using the above-mentioned boundary conditions we can simplify the result of equation (7) to the depth-averaged continuity equation:

$$\frac{\partial \eta}{\partial t} + \frac{\partial h\bar{u}}{\partial x} + \frac{\partial h\bar{v}}{\partial y} = 0 \tag{9}$$

Integration of the left-hand side of the x -momentum equation over depth yields:

$$\begin{aligned} &\int_{-d}^{\eta} [\frac{\partial}{\partial t}u + \frac{\partial}{\partial x}(u^2) + \frac{\partial}{\partial y}(uv) + \frac{\partial}{\partial z}(uw)]dz \\ &= \frac{\partial}{\partial t}(\mathrm{h}\bar{u}) + \frac{\partial}{\partial x}(\mathrm{h}\bar{u}^2) + \frac{\partial}{\partial y}(\mathrm{h}\bar{\bar{u}}\bar{\bar{v}}) \end{aligned} \tag{10}$$

Integrating the left-hand side of the y -momentum equation yields a similar result. Finally integration of the right-hand side of the horizontal momentum equation over depth yields:

$$-\rho gh\frac{\partial \eta}{\partial x}+\tau_{sx}-\tau_{bx}+\frac{\partial}{\partial x}\int_{-d}^{\eta}\tau_{xx}dz+\frac{\partial}{\partial y}\int_{-d}^{\eta}\tau_{xy}dz$$
$$-\rho gh\frac{\partial \eta}{\partial y}+\tau_{sy}-\tau_{by}+\frac{\partial}{\partial x}\int_{-d}^{\eta}\tau_{xy}dz+\frac{\partial}{\partial y}\int_{-d}^{\eta}\tau_{yy}dz \quad (11)$$

Where τ_{sx},τ_{sy} and τ_{bx},τ_{by} represent the turbulent stresses at the free surface and the ocean bottom respectively.

Combining the depth-integrated continuity equation with the depth integrated horizontal momentum equation, the nonlinear SWE reads:

(12)

$$\frac{\partial \eta}{\partial t}+\frac{\partial h\bar{u}}{\partial x}+\frac{\partial h\bar{v}}{\partial y}=0$$

$$\frac{\partial}{\partial t}(\mathrm{h}\bar{u})+\frac{\partial}{\partial x}(\mathrm{h}\bar{u}^{2})+\frac{\partial}{\partial y}(\mathrm{h}\bar{\bar{u}\bar{v}})+fu=-\rho gh\frac{\partial \eta}{\partial x}+\tau_{sx}-\tau_{bx}+\frac{\partial}{\partial x}\int_{-d}^{\eta}\tau_{xx}dz+\frac{\partial}{\partial y}\int_{-d}^{\eta}\tau_{xy}dz \quad (13)$$

$$\frac{\partial}{\partial t}(\mathrm{h}\bar{v})+\frac{\partial}{\partial y}(\mathrm{h}\bar{v}^{2})+\frac{\partial}{\partial x}(\mathrm{h}\bar{\bar{u}\bar{v}})+fv=-\rho gh\frac{\partial \eta}{\partial y}+\tau_{sy}-\tau_{by}+\frac{\partial}{\partial x}\int_{-d}^{\eta}\tau_{xy}dz+\frac{\partial}{\partial y}\int_{-d}^{\eta}\tau_{yy}dz$$

The surface stress, bottom friction and other terms have to be determined on a case-by-case basis. The parameterization of the friction parameters will be discussed in more details in Chapter 3.

As result of the long wavelength, tsunamis behave like shallow-water waves that move through the open ocean at a speed given by the following formula:

$$c=\sqrt{gh} \quad (14)$$

Where c, g and h represent the wave celerity, gravitational acceleration and the water depth respectively.

The 2D SWE is the governing equation describing the propagation characteristics of tsunamis. This equation forms the basis of many tsunami models including the H_2Ocean tsunami model which will be used for modelling the Chilean Tsunami.

The computed surface elevations and velocities will be used as input for the energy flux analysis. The derivation of the energy flux equations will be given the following section.

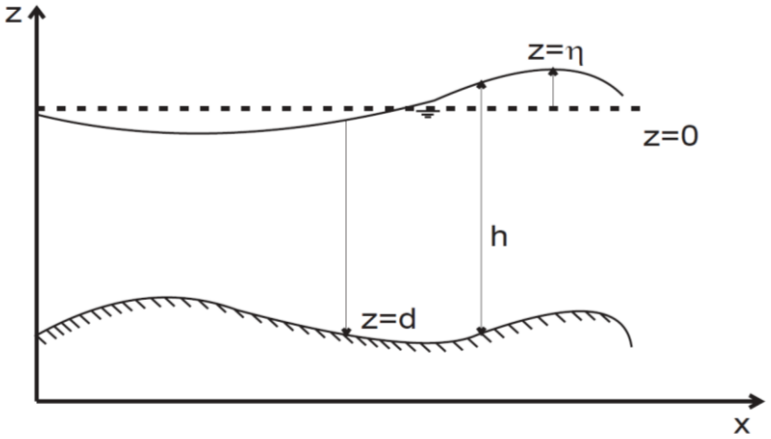

Figure 2.2: Vertical planar view of the ocean section, with bottom and free surface (Cui, Pietrzak, & Stelling, 2010)

2.2. Energy flux method

The energy flux in alongshore and cross-shore direction will be derived from the 2D SWE in the first section of this paragraph. Then the limitations and possibilities of this method will be discussed in the last section of this paragraph.

2.2.1. Derivation of the energy flux equation

The starting point of the derivation of the energy flux equations is simplifying the momentum conservation equations, Equation (2), and the continuity equation, Equation (3), to the following form (Kowalik & Murty, 1993):

$$\begin{aligned} &\frac{\partial \eta}{\partial t}+\frac{\partial h\bar{u}}{\partial x}+\frac{\partial h\bar{v}}{\partial y}=0 \\ &\rho\left(\frac{\partial u}{\partial t}+u\frac{\partial u}{\partial x}+v\frac{\partial u}{\partial y}\right)=-\rho g\frac{\partial \eta}{\partial x}-\frac{\tau_{bx}}{h} \\ &\rho\left(\frac{\partial v}{\partial t}+u\frac{\partial v}{\partial x}+v\frac{\partial v}{\partial y}\right)=-\rho g\frac{\partial \eta}{\partial x}-\frac{\tau_{by}}{h} \end{aligned} \tag{15}$$

This equation will be used to construct the energy conservation equation. In the above set of equations only the bottom stresses τ_{bx} and τ_{by} are used. The free surface stress is assumed to be negligible compared to other terms. The last step, in order to derive the energy balance equation, is multiplying the x-momentum equation by hu, the y-momentum equation by hv and the continuity equation by $\rho g\eta$:

$$\begin{aligned} &\rho g\eta\left(\frac{\partial \eta}{\partial t}+\frac{\partial h\bar{u}}{\partial x}+\frac{\partial h\bar{v}}{\partial y}\right)=0 \\ &\rho hu\left(\frac{\partial u}{\partial t}+u\frac{\partial u}{\partial x}+v\frac{\partial u}{\partial y}\right)=-\rho ghu\frac{\partial \eta}{\partial x}-\tau_{bx}u \\ &\rho hv\left(\frac{\partial v}{\partial t}+u\frac{\partial v}{\partial x}+v\frac{\partial v}{\partial y}\right)=-\rho ghv\frac{\partial \eta}{\partial x}-\tau_{by}v \end{aligned} \tag{16}$$

Adding the resulting equation on both sides and rewriting with the aid of factorisation, we get:

$$\frac{1}{2}\frac{\partial}{\partial t}(\rho \mathrm{g}\eta^2 + \rho h(u^2+v^2)) + \frac{\partial}{\partial x}(\rho uh(\frac{1}{2}(u^2+v^2)+\mathrm{g}\eta)) + \frac{\partial}{\partial y}(\rho vh(\frac{1}{2}(u^2+v^2)+\mathrm{g}\eta)) = \tau_{bx}u + \tau_{by}v \quad (17)$$

In this equation various energy quantities could be recognized:

1. $e_k = \frac{1}{2}\rho h(u^2+v^2)$ indicates the surface density of the kinetic energy.
2. $e_p = \frac{1}{2}\rho g\eta^2$ denotes the surface density of the potential energy.
3. The second and third term represent the components of a horizontal energy flux.

$$E_h = \begin{cases} E_x = \rho uh(\frac{1}{2}(u^2+v^2)+\mathrm{g}\eta) \\ E_y = \rho vh(\frac{1}{2}(u^2+v^2)+\mathrm{g}\eta) \end{cases} \quad (18)$$

4. The terms on the right-hand side of the energy balance equation represent the energy dissipation through bottom stress.

2.2.2. Possibilities and limitations of the energy flux quantity

The main advantage of the energy flux method is its directional property. This property enables us to identify the horizontal structure of the tsunami wave propagation. Where the surface motion is solely defined by the wave height, the energy flux is defined by the total depth, velocity and the flux of kinetic energy. The advantage becomes clear when acknowledging that the sign of the energy flux is purely determined by the direction of the velocity, a proof of this property is attached in Appendix A. This property allows us to separate the alongshore migrating (edge)waves from the cross-shore propagating waves. Additionally it allows us to distinguish for the across-shore and alongshore energy flux, i.e. E_x and E_y, whether the wave energy is transported in the positive or negative direction. This enables us to trace waves and asses the influence of bathymetric features on the wave propagation.

It is worth mentioning that the advantage of splitting the energy flux in along-shore and cross-shore component comes at a certain price. The limitation of this method is that the quantity E_x is blind for wave energy with a pure north-south orientation. The reverse obviously holds for E_y. This is due to the fact that the perpendicular velocity doesn't occur as an extra term in either quantities. In practise this implies that a pure north-south directed wave deflected perpendicularly will lose all its energy instantly.

The computations and implementation of the energy flux will be discussed in more details in Chapter 4. The results of the energy flux analysis will be discussed in the result section of this report.

2.3. Refraction

Yamazaki and Cheung (2011), Geist (2013) and Rabinovich et al. (2006) suggest that wave trapping is a result of wave refraction over the continental margin. we therefore describe qualitatively the physics behind wave trapping in coastal regions through wave refraction, following the discussion by Holthuijsen (2007).

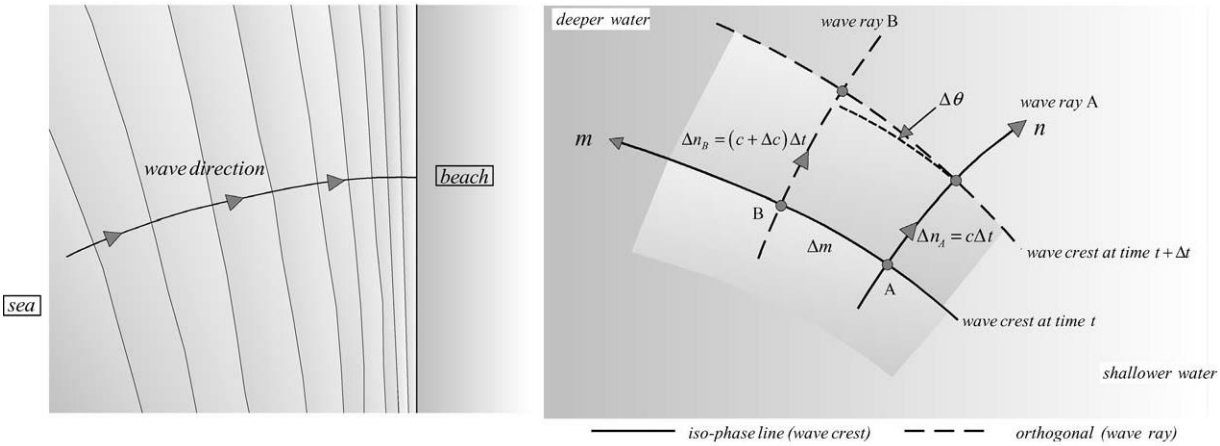

Figure 2.3: An obliquely incoming wave always turns to the region with lower propagation speed i.e. shallower water.

All types of waves, whether they are light waves, sound waves or water waves, may undergo refraction when they travel from a medium in which they have a higher speed into one in which they have a lower wave speed. The velocity of shallow water waves is proportional to the water depth. So a wave moves faster in deeper water than in shallower water. So a wave crest, as visualised in Figure 2.3, moves over a larger distance in deeper water than it does in shallower water. The effect of refraction is that the wave refracts (turns) towards the region with shallower water. For infinitesimally small differences in the wave celerity the following differential equation can be derived (Holthuijsen, 2007):

$$\frac{d\theta}{dn} = -\frac{1}{c}\frac{\partial c}{\partial m} \tag{19}$$

With c the wave celerity, m the iso-phase line (wave crest), n the coordinate normal to the wave crest i.e. propagation direction and θ represents the directional turning of the crest, see Figure 2.3. For a straight coast with uniformly sloping bathymetry i.e. parallel depth contours there exists a simple solution of the geometric-optics approximation, Equation (19), also known as Snel's Law:

$$\frac{\sin(\theta)}{c} = \text{constant} \tag{20}$$

The wave speed of a wave approaching the coast will decrease when the water depth decreases. The angle θ in Snel's Law, which is the angle between the wave ray and the normal to the straight and parallel depth contours, should also decrease to keep the ratio of Snel's Law constant. This implies that the wave will be refracted to shallower water. After reflection at the coast the wave will propagate in the seaward direction, the wave will accelerate due to increasing water depth. The wave angle θ should decrease to compensate the increasing wave speed c, to keep the ratio constant. This implies that the wave will be again refracted towards shallower water. The reflection and refraction of long wave waves on a uniformly sloping beach is what creates a coastally trapped edge wave (LeBlond & Mysak, 1978).

3. Model description and tsunami simulation

This chapter gives an overview of the steps in simulating the tsunami with H_2Ocean, a numerical tsunami finite volume model. H_2Ocean model requires the bathymetry, initial field and an unstructured mesh as input to simulate the 2010 Chile tsunami. The next paragraph will discuss the procedure followed to generate a depth dependent mesh. Subsequently information is given on the available bathymetry and uplift data and how this data is used as input for the model. In the last paragraph the model parameters are discussed.

3.1. Governing equation

The governing equations that model the tsunami wave propagation which is solved by the model are the 2D shallow water equations (Cui, Pietrzak, & Stelling, 2010):

$$\begin{aligned} &\frac{\partial \eta}{\partial t} + \nabla \cdot [(\mathrm{d} + \eta)\mathbf{u}] = 0 \\ &\frac{\partial \mathbf{u}}{\partial t} + \mathbf{u} \cdot \nabla \mathbf{u} + f\mathbf{k} \times \mathbf{u} = -g \nabla \eta \end{aligned} \tag{21}$$

η represents the water level, $\mathbf{u}$ the depth-averaged horizontal velocity with components (u, v), d the reference water depth, f the Coriolis parameter with $\mathbf{k}$ a unit vector in vertical direction and ∇ the two dimensional gradient operator. In the shallow-water equation the vertical accelerations have been neglected resulting in the reduction of the vertical momentum equation to its hydrostatic-pressure equivalent. The underlying assumption is that for long waves the depth of the fluid is small compared to the wave length.

H_2Ocean is a numerical model that solves the 2D-SWE numerically. A numerical model can only solve differential equations, such as equation (21), if it is discretized into an algebraic set of equations. H_2Ocean is a finite volume unstructured grid ocean model. It is a finite volume analogue of the $P_1 - P_1^{NC}$ finite element discretization, which has the water elevation located on the vertex and the velocity vectors located on the middle of the edge (Hanert, et al., 2005). The finite volume version of the model was developed to simplify the implementation of the flooding and drying routines, (Cui, Pieterzak, & Stelling, A finite folume analogue of the P1^NC-P1 finite element: With accurate flooding and drying , 2010), (Cui, Pietrzak, & Stelling, 2012).

3.2. Non-uniform space partitioning and boundary condition

3.2.1. Space partitioning

The first step to simulate a tsunami with H_2Ocean is to divide the solution space into a number of small triangles called elements. Each element is formed by the connection of its nodes (vertices) by edges. The elements are unstructured, which provides a better representation of complex boundaries such as coastlines. It also facilitates the opportunity to generate a depth-dependent mesh-resolution to a degree not possible with nested or curvilinear grids. For this research two different meshes are generated using a C-based mesh generator, TRIANGLE by Shewchuk (1996). The first mesh is generated for the purpose to simulate accurate flooding and tsunami propagation along the Chilean coast. This relative small region spans from Valparaiso (32° S) to Corral (40° S). The

second mesh is generated to be able to validate the model setup in the far field with DART buoys and spans the same region as the ETOPO1 Bathymetry data. Both meshes were generated following the procedure of generating a basic triangulation containing all boundary nodes and the restriction of edge lengths not larger than the coarsest acceptable resolution. In the second step this triangulation is refined using the following depth-dependent element area restriction:

$$A \leq h / \alpha \tag{22}$$

Where A, α and h represent the triangular element area, a user defined restriction and the water depth or topography height respectively. The resulting meshes were smoothed to improve the overall mesh quality. The coarsest resolution of the Pacific-wide mesh is 14 km in the deep ocean to 1 km near the epicentre of the earthquake. The resolution of the regional mesh ranges from 1 km in the deep water to a high resolution of 80 m near the coast and on land. Both meshes count approximately 1.2 million nodes. A summary of the mesh characteristics is given in Table 3.1. Figure 3.1 visualizes the mesh representing the Bay of Concepción.

Table 3.1: Mesh characteristics

Parameter	Pacific wide mesh	Regional mesh
Number of nodes	1 174 391	1 170 390
Refining restriction α	-	0.001
Resolution [m]	14 000 – 1 000	1 000 - 80

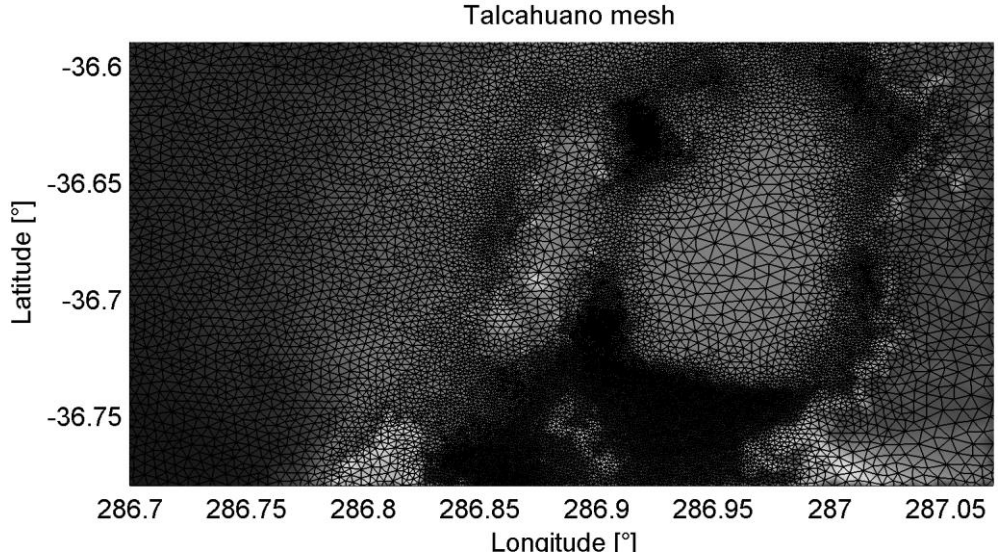

Figure 3.1: Generated mesh using Triangle (The coastal bathymetry data contains sensitive information, therefore not all details of the bathymetry has been shown in this version of the figure).

3.2.2. Boundary condition

To solve the 2D-SWE boundary conditions are required at all boundaries of the simulated domain. H_2Ocean enables 3 different types of boundaries i.e. open and closed boundaries, and a so called Dirichlet boundary condition. In the generated mesh all boundaries on land are set as closed (solid) boundaries and all boundary vertices in the open ocean are set as open boundaries. This latter setup allows waves to exit the domain without reflecting back into the domain.

3.3. Input files

3.3.1. Bathymetry

Bathymetry and topography data of Chile are provided by Pontificia Universidad Católica de Chile. The bathymetry data of Chile has an overall resolution of 30 arc-sec (1000 m) and is based on the General Bathymetric Chart of the Ocean (GEBCO) data set (GEBCO, 2008). This dataset has been improved by the Hydraulic department using nautical charts and bathymetric measurements for the Talcahuano region. The achieved resolution for Talcahuano bay is 80 m. Topography data of the Pacific region is retrieved from ETOPO1 dataset and has a resolution of 1 arc-min (2000 m). The boundary limits of the used bathymetry datasets are described in Table 3.2. The GEBCO bathymetry dataset has been visualised in Figure 3.2.

Table 3.2: Bathymetry data, boundary coordinates indicates top-right and bottom-left boundary corner coordinates.

Region	Boundary coordinates	Resolution
Pacific	20° N/130° W - 40° S/70° W	1 arc-min
Chile/Pacific	20° S/120° W - 60° S/60° W	30 arc-sec
Talcahuano Bay	36.59° S/73.25° W -36.78° S/72.93° W	80 m

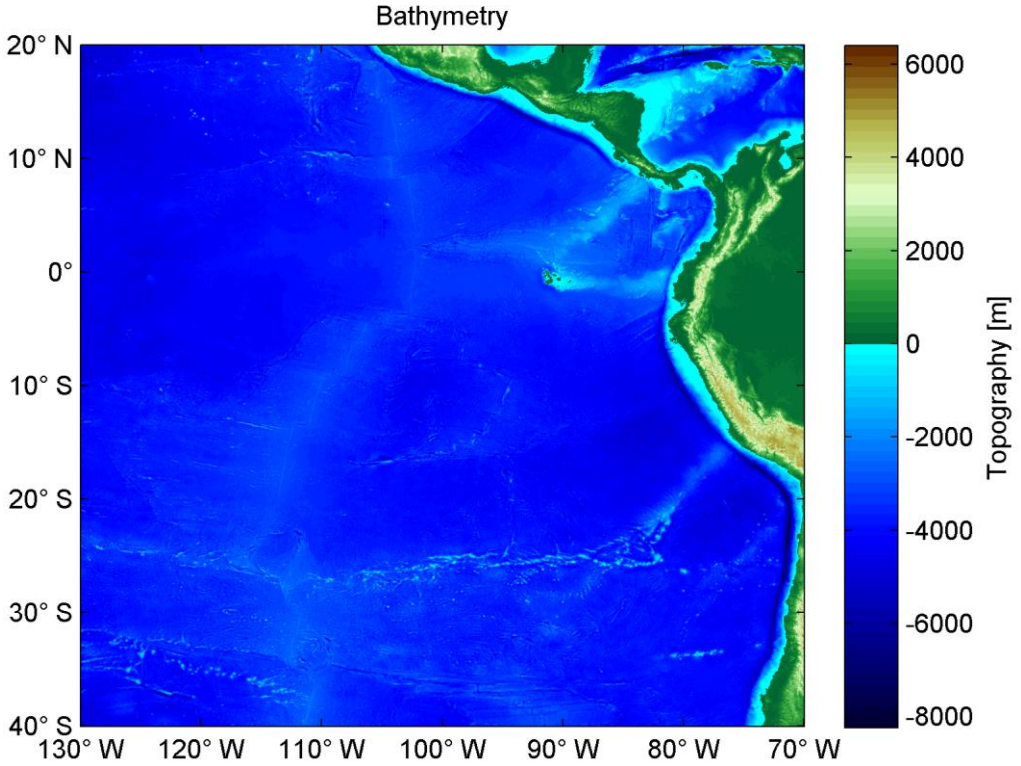

Figure 3.2: Visualisation of the bathymetry data for the pacific ocean region.

3.3.2. Initial field

There are many studies on the rupture process of the 2010 Chile earthquake using both geodetic and teleseismic measurements. Three different initial fields will be used as input for the tsunami simulation. The initial field that follows Moreno's GPS inversion (Moreno, Rosenau, & Oncken, 2010), the initial field by Delouis et al. (2010) is provided by Broerse and the initial field derived by Vigny et al. (2011) and provided by Socquet.

The vertical displacement, visualised in Figure 3.3, shows that all initial fields predict two regions of high vertical displacement. The main difference between Delouis and Vigny & Moreno is the location of the asperities relative to the trench; Vigny and Moreno have their maximum slip closer to the trench than Delouis. The location of the asperities, relative to the trench, is of great importance to the tsunami arrival times and the amplitude of edge waves (Geist, 2013). For the 2010 Tohoku-Oki earthquake, concentration of the majority of the slip near the trench resulted in accurate tsunami simulation results (Hooper, et al., 2012). It is therefore expected that Moreno's and Vigny's earthquake solution will also produce better results. For the simulation we assume an instantaneous earthquake rupture and incompressible fluid. This latter assumption implies that the ocean surface will mimic the uplift with a ratio of one.

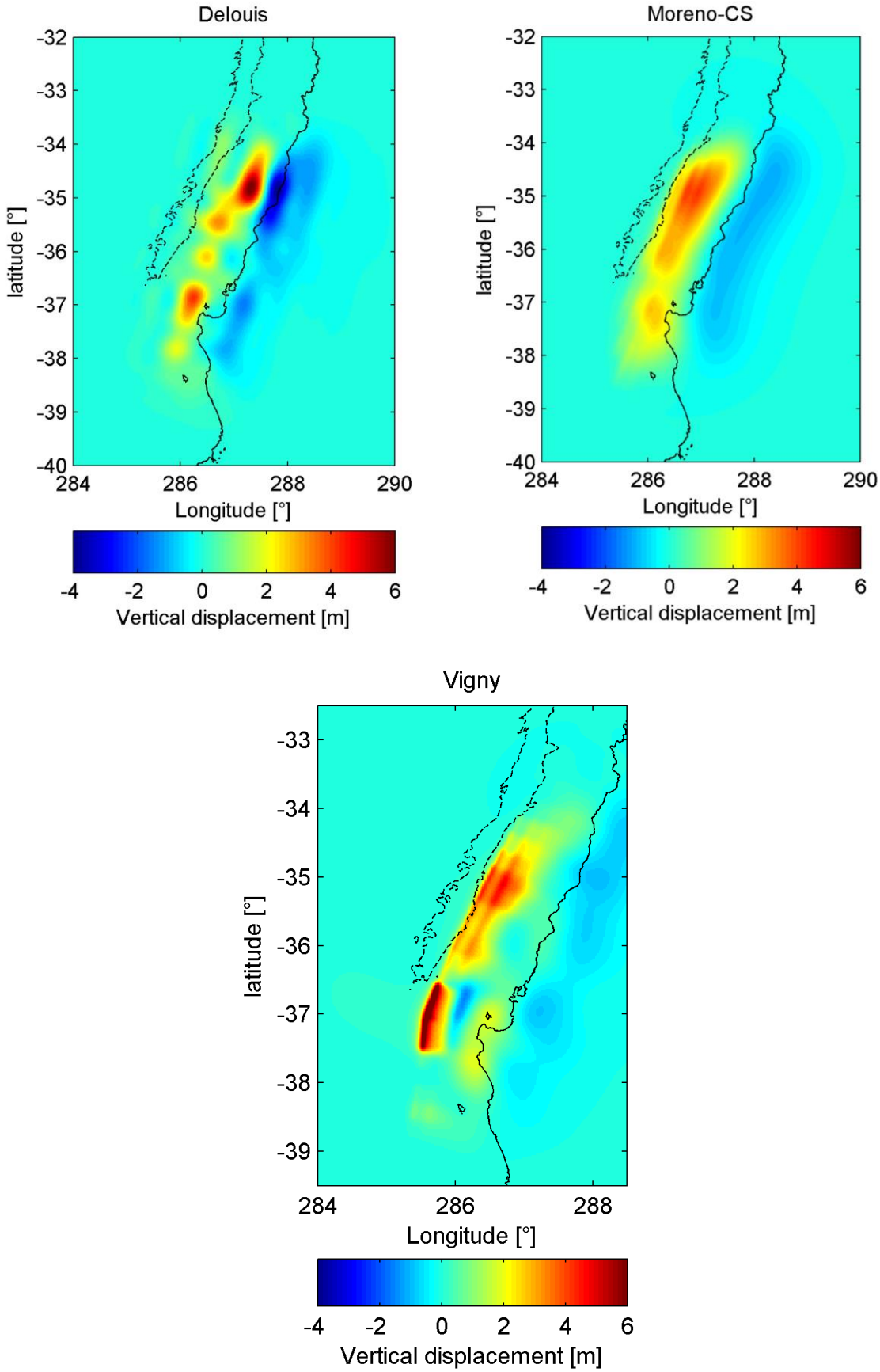

Figure 3.3: Initial field according to Delouis, Moreno and Vigny describing the initial uplift.

3.3.3. Interpolation on mesh

The last step in the preparation of the input files for the simulation is the interpolation of the initial uplift and bathymetry to the generated mesh. The bathymetry dataset has three different levels of resolution. Because the computational effort is much higher for interpolation of scattered data the bathymetry is first converted to a grid. Then interpolation is done by a grid-based interpolation method of Matlab. In other words; bathymetry and initial uplift data (xyz-format) were first interpolated to a grid. From this point bilinear interpolation method is applied to determine the depth and uplift at the mesh nodes.

For each node on the mesh the depth $z_1,...,z_4$ is known at the corner positions $p_1,...,p_4$ of an enclosing square. The depth z_i at location p_i is determined by the parameters $(p_1,z_1);\ ...\ ;(p_4,z_4)$ and can be written as follows:

$$z_i = w_1 \cdot z_1 + ... + w_4 \cdot z_4 \tag{23}$$

The position p_n, $n = 1,...,4$ in a plane has an x_j and a y_j component, $j = 1,2$. So the weights in equation (23) could be determined by the perpendicular distance to the corners of the square:

$$\begin{aligned} w_1 &= \frac{(x_2 - x_i)(y_2 - y_i)}{(x_2 - x_1)(y_2 - y_1)} \\ w_2 &= \frac{(x_i - x_1)(y_2 - y_i)}{(x_2 - x_1)(y_2 - y_1)} \\ w_3 &= \frac{(x_2 - x_i)(y_i - y_1)}{(x_2 - x_1)(y_2 - y_1)} \\ w_4 &= \frac{(x_i - x_1)(y_i - y_1)}{(x_2 - x_1)(y_2 - y_1)} \end{aligned} \tag{24}$$

The same approach is used to determine the initial uplift η_i at the mesh-node number i. Finally the bathymetry is adjusted to account for the earthquakes coseismic uplift and subsidence of the earthquake rupture:

$$d_i = z_i + \eta_i \tag{25}$$

After preparing the input files in the format compatible with the model the simulation parameters have to be set in a so called control file. This latter part will be discussed in the following paragraph.

3.4. Model parameters

For this simulation the model outputs the water level at each node every 30 seconds. The modelling parameters used for the tsunami simulations are summarized Table 3.3.

The Courant-Friederichs-Lewy (CFL) condition, equation (26), is a condition necessary to guarantee stability while solving the 2D-SWE numerically. The consequence of this condition is that the time step depends on the wave velocity and the mesh resolution. For high wave celerity the time step will be automatically reduced to prevent incorrect results as consequence of waves overshooting nodes. The initial time step was set to 5 seconds because the wave velocity is assumed to be zero at $t = 0$.

$$\frac{u\Delta t}{\Delta x}+\frac{v\Delta t}{\Delta y}\le CFL_{\max} \tag{26}$$

The generated mesh is defined in a geographic coordinate system which allows the model to apply a latitude dependent Coriolis force. For the flooding mesh which spans a region with latitude ranging from 32° S to 40° S a latitude averaged Coriolis force may suffice. However, the Pacific wide mesh spans a much larger region with latitudes ranging from both sides of the equator. This implies that this fictitious force will change sign when crossing the equator. So a latitude dependent representation of this force is indispensable for this simulation.

The hydrostatic assumption is applied for our simulations. This means that the model ignores the effects of dispersion due to non-hydrostatic physics. We expect that these effects will be negligible because the dominant wavelengths are much larger than the water depth (Pieterzak, et al., 2007).

In Chapter 2 it is mentioned that the surface stress, bottom friction and other boundary-related terms have to be determined on a case-by-case basis (Vreugdenhil, 1994). In this case we don't model surface stresses which may result from wind and other atmospheric conditions. The effect of atmospheric conditions on the tsunami propagation is expected to be negligible. In contrast to surface stress, the bottom friction is one of the dominant dissipation mechanism of the wave energy. The parameterisation of bottom friction is based on Chezy's approach. The shear stress is experimentally estimated as:

$$\begin{aligned}\tau_x &\approx Cu\sqrt{u^2+v^2}\\ \tau_y &\approx Cv\sqrt{u^2+v^2}\end{aligned} \tag{27}$$

This formula is used with the Manning's Roughness Coefficient:

$$C=\frac{gn^2}{\sqrt[3]{d+\eta}} \tag{28}$$

Where C and n are the Chézy Coefficient and the Manning's Roughness Coefficient respectively. It is worth noting that Manning's coefficient n ranges from 0.01 for smooth concrete to 0.06 for concrete channels. For tsunami simulations a value of approximately $n=0.025$ is frequently used (Harig, Pranowo, & Behrens, 2008). The model parameters used for our simulations are summarised in Table 3.3.

Table 3.3: Model parameters used for the simulation

Computation parameter	Setup
Time step (initial)	Variable (5 sec)
Simulation time	6 h / 15 h
Max_CFL	0.8
Coriolis	$2\Omega\sin(\theta)$
Manning coefficient	0.025
Non-hydrostatic	False

4. Observation data and methods

This chapter provides an explanation of the available data used for validation purposes and the methods applied to process the tsunami-simulation results. In the first paragraph the preparation of tide gauge observations is discussed. The subsequent paragraph explains the methods used to process the DART buoy observations. Then the method, used to determine the best earthquake source model, is presented. Finally the implementation to compute the energy flux from the computed surface elevations is explained in the last paragraph.

The location of the DART buoys and tide gauges are visualized in the following Figure 4.1.

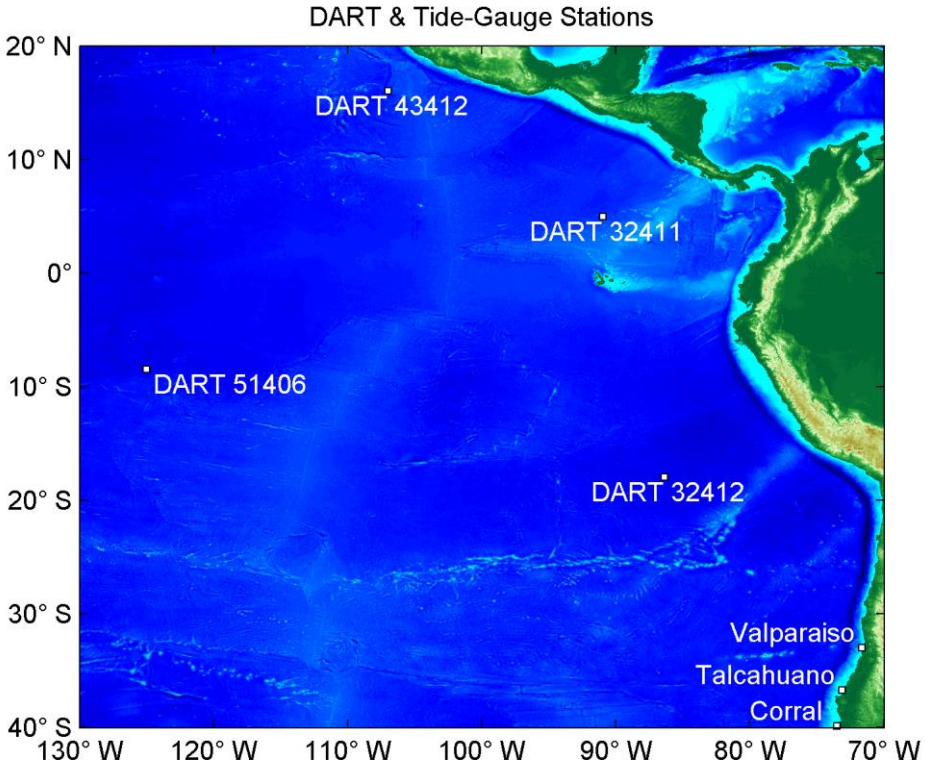

Figure 4.1: Location of DART buoys and coastal tide gauges

4.1. Data near field

The tide gauges along the Chilean coast will be used in order to assess the model setup. The tide gauge observations, which are located in the domain of the flooding mesh, are listed in Table 4.1. The tide gauge observations will be used for validating the model setup, and assessing the initial fields. Moreover, they give information about the tsunami arrival times and number of incoming waves. The tide gauges along the coast of Chile are pressure gauges at the seabed with a sampling rate of 2 minutes. It is expected that the sampling rate of 2 minutes is suitable to detect tsunami waves, as the tsunami wave period ranges between 5 minutes and 120 minutes (NOAA, 1991).

Table 4.1: Stations in the near field tsunami simulation region and sampling rate.

Station name	Sampling rate [min]
Talcahuano	2.2
Corral	2.0
Valparaiso	2.1

4.1.1. Data processing

The tsunami event of 2010 persisted long enough that the influence of the tide is significantly present in the sea level observations. The H_2Ocean tsunami model doesn't take the tide in to account. For this reason the tide gauge observations have to be corrected for the tidal motion.

In order to correct the observations for the tide a Matlab-based tide fitting toolbox is used which is developed by Grinsted (2008). This method assumes that the tidal motion satisfies the following algebraic equation:

$$y_i = A_0 + \sum_{j=1}^{M} A_j \cos(f_j t_i + \varphi_j) \tag{29}$$

With y_i representing the observation at time t_i and A_0 the mean sea level. The summation term represents the tidal constituents present in the tidal signal for the unknown amplitude A_j and phase φ_j corresponding to the tidal constituent $j = 1, \mathrm{M}$. The frequency f_j is known for many tidal constituents and can be found in the literature. The amplitude and phase of each constituent is estimated by linear least squares method. To solve the equation by the least squares method, the term representing the tidal motion has to be rewritten to the following form (Foreman & Henry, 1989):

$$A_j \cos(f_j t_i + \varphi_j) = C_j \cos(f_j t_i) + S_j \sin(f_j t_i) \tag{30}$$

Where

$$A_j = \sqrt{C_j^{\,2} + S_j^{\,2}} \text{ and } \varphi_j = \arctan(\frac{S_j}{C_j})$$

The aforementioned linearized equation can be written in its matrix-vector equivalent:

$$y_i = A\mathbf{x} + \boldsymbol{e} \tag{31}$$

Where y_i , $\mathbf{x}$ and $\boldsymbol{e}$ are vectors of observations, the C_j and S_j coefficients and the residuals respectively. The design matrix and unknown vector $\mathbf{x}$ are written for the first tidal constituent.

$$A\mathbf{x} = \begin{bmatrix} 1 & \cos(f_1 t_1) & \sin(f_1 t_1) \\ \vdots & \vdots & \vdots \\ 1 & \cos(f_1 t_N) & \sin(f_1 t_N) \end{bmatrix} \begin{bmatrix} A_0 \\ C_1 \\ S_1 \end{bmatrix} \tag{32}$$

The normal equation that results from minimizing $\boldsymbol{e}^T\boldsymbol{e}$ is:

$$A^T A\mathbf{x} = A^T \boldsymbol{y} \tag{33}$$

And its solution is given by:

$$\mathbf{x} = (A^T A)^{-1} A^T \boldsymbol{y} \tag{34}$$

The solution of this system minimizes the residuals between the model and the observation which yields the best fit. The output is the amplitude and phase for each fitted constituent which can be used to predict the tide for the next epoch. This method uses ordinary least squares method to estimate the tidal parameters. It is necessary to use a few weeks of observations to obtain a reasonable prediction of the tidal signal. This latter part will be discussed in more details in the last section.

4.2. Data in the far field

The deep-ocean assessment and reporting of tsunamis system (DART) consists of an anchored sea floor bottom pressure recorder (BPR) and a moored surface buoy for real-time communication (Gonzales, Milburn, Bernard, & Newman, 1998). The BRP collects temperature and pressure with a sampling rate of 15 seconds. The temperature measurements are used to correct for temperature influences when converting the pressure to sea-surface heights. The system has two reporting modes; standard and event. In standard mode the DART buoy transmits the averaged sea-surface heights at 15 minutes intervals. In the event mode, 15 seconds values are transmitted during the initial few minutes, followed by 1 minute averages. The sampling rate of the DART buoy observation is small enough to reconstruct all wave characteristic of the fast propagating tsunami wave.

4.2.1. Data pre-processing

In the previous paragraph it is mentioned that DART measurements are inhomogeneous in the temporal domain. The sea level data has to be pre-processed to a temporally homogenous dataset. This is done by creating a homogenously spaced time vector with time increments depending on the highest temporal resolution i.e. 15 seconds. Subsequently the sea surface heights are (linearly) interpolated to the epochs with missing measurements. After homogenising the observations the tide has to be eliminated from the signal. The tidal amplitude is expected to be bigger than the tsunami height in the far field. The method used to remove the tide applied for the tide gauge observations is not suitable because the RMS of several centimetres is as big as the tsunami signal itself. For this reason the tide will be removed by means of spectral filtering.

4.2.2. Spectral Analysis and filtering

It is convenient to transform the time series of the surface elevation to frequency domain to be able to acquire more knowledge of the spatial variation of the wave field. Besides this we also use spectral filtering to correct the data from the tidal signal and other undesired signals such as (infra)gravity waves. We start this discussion by briefly introducing the theory behind the, built-in function of Matlab, used for this analysis called Fast Fourier Transform (FFT).

The FFT function is based on the concept of Discrete Fourier Transform (DFT). This function requires the time series of the surface elevation η_n, the surface elevation at time $t = n$. The DFT of this is then defined as follows:

$$\mathrm{H}_m = \mathcal{F}\{\eta_n\} = \sum_{n=0}^{N-1} \eta_n \omega_N{}^{-mn}$$
$$\omega_N{}^{-mn} = e^{-i2\pi nm/N} \tag{35}$$

Where H_m represents the m-th DFT output component, m denotes the index of the output counting the same length as the input sequence and N is the number of samples of the input sequence and the number of samples of the frequency points in the DFT-output. In essence, the DFT transforms the time series, which is a function of time and space, to a quantity (amplitude spectrum) which is a

function of frequency and space. The fact that the amplitude spectrum has the same length as the input signal is a bit ambiguous. The reason for this is that the DFT actually checks for a correlation between a set of given frequencies and the input signal:

$$f_m = \frac{m}{N} f_s \tag{36}$$

Where f_m denotes the DFT analysis frequency and f_s the sampling frequency of the input sequence. Even though the index m of the DFT output denotes the frequency-domain range of the signal, one has to be careful when interpreting it. Equation (36) implies that the DFT analysis frequency depends on the sampling frequency of the input signal. This implies that the frequency range is scaled by a factor depending on the sampling frequency of the input signal.

Before going into the details of some useful properties of the DFT a brief discussion of the classification of (ocean) waves, as proposed by Munk (1950), will be given. Figure 4.2 illustrates the broad spectrum of waves present in the open ocean with wave period ranging from deci-seconds to several days. The figure shows that tsunamis (earthquakes) are classified as long period waves with periods between 5 and 120 minutes (NOAA, 1991). It is worth noting that the same wave periods could also be generated by storms. This makes it almost impossible to distinguish the tsunami-waves from storm-waves if such a storm occurs at the same time of the earthquake. However, the obtained model fit at all Dart buoys indicate that it is unlikely that such a storm occurred during the passage of the tsunami wave.

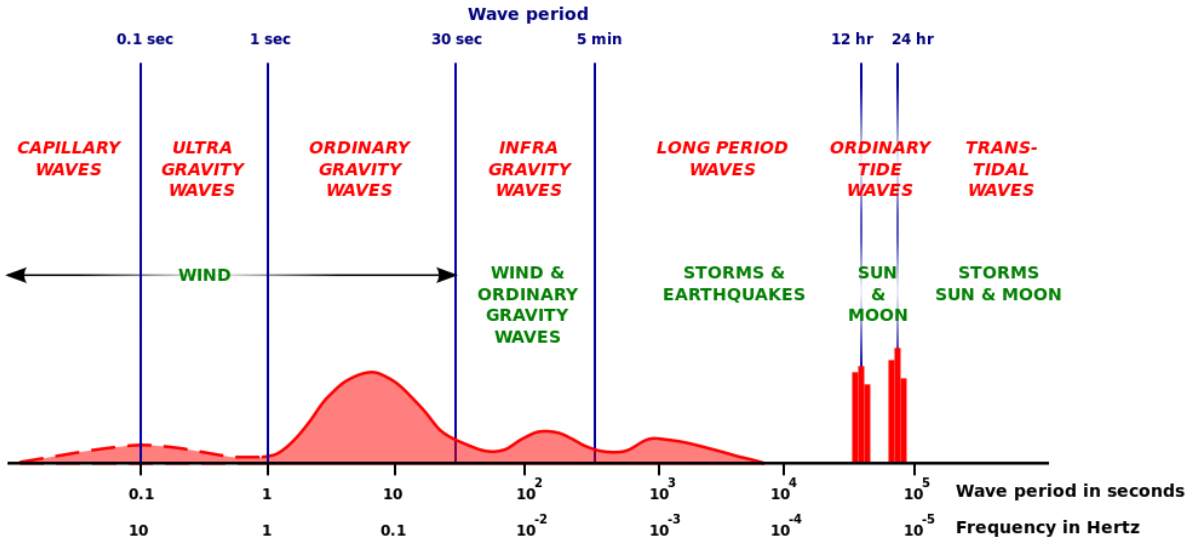

Figure 4.2: Classification of the spectrum of ocean waves according to wave period. Source: (Munk, 1950)

In this last part of this paragraph some properties of DFT will be discussed. Please note that we confine ourselves to discuss only the properties which are applied for filtering the data. Completeness is one of the advantageous properties of the discrete Fourier transform. It implies that the DFT is an invertible, linear transformation:

$$\eta_n(x,y,t) \underset{\mathcal{F}^{-1}\{\mathrm{H}_m\}}{\overset{\mathcal{F}\{\eta_n\}}{\rightleftarrows}} \mathrm{H}_m(x,y,f_m) \tag{37}$$

Where $\mathcal{F}^{-1}\{\mathrm{H}_m\}$ denotes the inverse discrete Fourier transform (IDFT):

$$\eta_n = \mathcal{F}^{-1}\{\mathrm{H}_m\} = \frac{1}{N}\sum_{m=0}^{N-1} \mathrm{H}_m {\omega_N}^{mn}$$
$${\omega_N}^{mn} = e^{i2\pi nm/N} \tag{38}$$

Another advantage of processing data in the frequency domain is that the convolution in the time domain is equivalent to a multiplication in the frequency domain. So in theory we could filter the data from the tide by multiplying all m -indices, which correspond with low frequency waves such as the tide, of the DFT of the sea level observations by zero:

$$\mathrm{H}_{filtered} = \mathbf{f} \cdot \mathrm{H}_m \tag{39}$$

Where $\mathbf{f}$ denotes the vector with filter coefficients:

$$\mathbf{f} \begin{cases} 1, & \mathrm{T}_w \in [5,120\rangle \\ 0, & \mathrm{T}_w \notin [5,120\rangle \end{cases} \tag{40}$$

With T_w the wave period. The period of tsunami waves ranges between 5 and 120 minutes (NOAA, 1991). By this multiplication we aim to filter the signal from all low frequencies such as the tide and all high frequency waves i.e. wind, ordinary- and infra-gravity waves.

During the procedure above one has to be very careful because we are dealing with time series. First of all the sequence must be a uniformly spaced time series. During the DFT and IDFT processes we can encounter problems such as aliasing and leakage. Aliasing, i.e. frequency ambiguity, is the problem which entails that we are not able to distinguish a frequency f_0 and a frequency $f_0 = f_0 + k \cdot f_s$ in a discretized signal (Figure 4.3). Aliasing is expected to be small since the sea surface observation are already discrete sequences with a sufficiently high sampling rate. In the frequency domain, a low temporal resolution manifest itself in spreading out (leakage) of a amplitude peak in one (frequency)bin into other bins. In other words the measured correlation at other frequencies than the actual frequency is non-zero. In practise the filtering process is done by trial and error until the desired signal is computed. Our goal is to compare the tsunami simulation results to the recordings. So all wave lengths that are not in the range of the tsunami wave period will be filtered out of the observations. The results of the filtering process of the DART buoys observations and the validation is discussed in the following chapter.

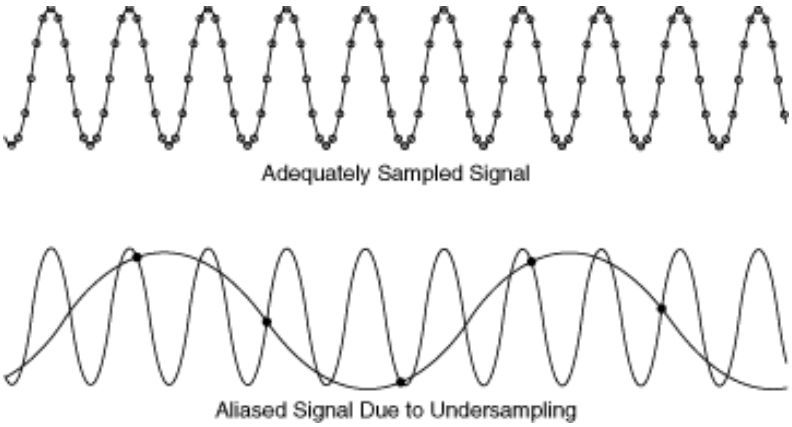

Figure 4.3: Aliasing as a consequence of undersampling (National Instruments , 2004).

4.3. Hypothesis testing

Three source models describing the vertical deformation of the Maule earthquake are available for this research. The wave propagation according to these uplift models have been simulated for several hours. Hypothesis testing will be used to determine quantitatively which available source model produces best tsunami results at observation sites.

The Hypothesis that will be considered in this research is on the mean of the misfit between the modelled and the observed tsunami signal. The hypothesis formulated in terms of condition equations (Teunissen, 2000) reads:

$$H_0 : B^T E\{\underline{y}\} = E\{\underline{z} - \underline{\eta}\} = 0 \tag{41}$$

Where B^T represents the condition matrix, $\underline{y}$ the vector of observables containing the modelled and observed sea surface heights, $\underline{z}$ the vector of observed sea surface heights and $\underline{\eta}$ the vector containing the modelled sea surface heights.

The appropriate test-statistic reads:

$$\underline{T}_{q=m-n} = \frac{\underline{\hat{e}}^T Q_y^{-1} \underline{\hat{e}}}{m-n} \tag{42}$$

With $\underline{\hat{e}}$ the residual vector that represents the difference between the modelled results and the observations at observation-sites, Q_y denotes the covariance matrix of the observables:

$$\underline{\hat{e}} = Q_y B (B^T Q_y B) B^T \underline{y} \tag{43}$$

$$Q_y = \begin{bmatrix} \sigma_O^2 & & & & & \\ & \ddots & & & 0 & \\ & & \sigma_O^2 & & & \\ & & & \sigma_M^2 & & \\ & 0 & & & \ddots & \\ & & & & & \sigma_M^2 \end{bmatrix} \tag{44}$$

Where σ_O^2 denotes the precision of the observations and σ_M^2 is a measure of the precision of the modelled sea surface heights. The precision of the observations are assumed to be 1 mm as proposed by the developer of the DART buoys (NOAA, 2006). We assumed that the precision of the tide gauges is the same as the precision of DART buoys. The model's precision is location dependent and has been estimated by the root-mean-square of the residuals between the modelled and observed sea surface heights (Willmont, et al., 1985):

$$\sigma_M = \sqrt{\frac{1}{m} \sum_{i=1}^{m} | z_i - \eta_i |^2} \tag{45}$$

Where m denotes the length of the observation vector. The estimates of the precision of the model and observations at all observation sites have been summarised in Table 4.2.

Table 4.2: The precision of the modelled and observed sea surface heights at observation site. The modelled precision also depends on the source model used for the tsunami simulation.

Station name	Delouis [cm]	Moreno [cm]	Vigny [cm]	Observations [cm]
DART 32412	2.54	2.44	2.51	0.1
DART 51406	3.17	3.09	2.56	0.1
DART 32411	1.03	1.16	1.11	0.1
DART 43412	1.56	1.70	1.55	0.1
Talcahuano	1.15	1.13	1.41	0.1
Valparaiso	0.87	1.02	1.01	0.1
Corral	1.07	1.01	0.97	0.1

The null hypothesis should be rejected if the value of the test statistic is larger than the critical value which equals the inverse of the Fisher-distribution with q degrees of freedoms:

$$\text{reject } H_0 \text{ if } \underline{T}_q > k_\alpha = \text{inv-}F(1-\alpha, q, \infty, 0) \tag{46}$$

Where k_α represents the critical value, for the significance level α which represents the probability of the right-hand tail. The results of the hypothesis testing is presented in the results section of this report.

4.4. Energy flux approach

We propose to use the energy flux according to the theory discussed in Chapter 2 to analyse the importance of edge waves and the role of bathymetric features on the tsunami impact along the coast of Chile. It is expected that splitting the flow field in perpendicular components representing the energy flux in cross-shore and along-shore will give more insight in the wave propagation.

As mentioned in Chapter 3, an unstructured mesh is required to simulate the tsunami. This means that the water level and velocity output for each epoch is a row vector. The complication encountered when computing the energy flux is not related to the rather simple equation representing the along-shore and cross-shore energy flux, but is associated with the way the model stores the velocity information. As mentioned in the previous chapter the velocity vectors are located at the middle of the edges. This implies the velocity vectors are taller in length than the bathymetry and surface level vectors, the number of vertices doesn't equal the number of edges in an unstructured mesh. Another consequence of unstructured meshes is that the numbering of nodes is unstructured. These difficulties force us to interpolate the velocities on the vertices prior to computing the energy flux. Interpolation in a vector field is a bit ambiguous when the interpolation is solely based on the scalar quantities representing the vector field. This ambiguity can be resolved by forcing the interpolated flow field to preserve the vorticity and divergence fields associated with the raw data (Schaefer & Doswell III, 1978). The error associated with it however is expected to be very small as we are dealing with long waves. Moreover the shallow water approximation already assumes divergence free vector field. As proven by Constantin & Johnson (2007) the assumption of a constant-vorticity solution for tsunami waves from deep water to shoreline is valid. So the straightforward interpolated flow field is justified by the aforementioned arguments.

The energy flux is implemented by simply computing the result of the following formula:

$$\begin{aligned} \mathbf{E}_x &= \rho \cdot (\mathsf{d} + \boldsymbol{\eta}) \circ \mathbf{u} \circ (\mathrm{g} \cdot \boldsymbol{\eta} + \frac{1}{2}(\mathbf{u}^2 + \mathbf{v}^2)) \\ \mathbf{E}_y &= \rho \cdot (\mathsf{d} + \boldsymbol{\eta}) \circ \mathbf{v} \circ (\mathrm{g} \cdot \boldsymbol{\eta} + \frac{1}{2}(\mathbf{u}^2 + \mathbf{v}^2)) \end{aligned} \tag{47}$$

It is worth noting that the bold letters denote column vectors and that the $\circ$ symbol denotes the Hadamard product. This product simply implies element-wise vector multiplication. The energy flux has been calculated for each epoch and for the entire wet domain. The dry nodes and nodes located in flooding area have been excluded from this computation. This energy formulation is not likely to be valid for flooded areas (Kowalik & Murty, 1993). Thereby this area is considered outside the area of interest.

Finally the energy flux has been visualised by generating maps of instantaneous energy flux for each epoch. The maps have been collected in order to generate a movie which enables us to trace certain waves to get more insight in the relation between wave (energy) propagation and bathymetric features, such as river canyons.

5. Validation and model selection

This chapter presents the results of the tsunami simulation at the observation location in both the near and far field. Subsequently the model that generates the most accurate tsunami signal will be determined by statistical hypothesis testing. The discussion starts with the presentation of the of the results of the tide gauge data processing.

5.1. Processing of the tide gauge observations

The least squares method is applied to estimate the amplitude and phase of the tidal signal at observation sites. For each tide gauge a period of 2 months or more is used to estimate the tidal parameters. The resulting analytical model of the tide, Equation (30), is used to predict the tidal signal during the tsunami. The tidal model fit at observation sites is illustrated in Figure 5.1. The degree to which the tidal model describes the variance of the tide is used as a measure of the performance i.e. the goodness of fit (GOF) of the tidal prediction.

$$GOF = \frac{var[A\mathbf{x}]}{var[\boldsymbol{y}]} = \frac{E[(A\mathbf{x} - \mu)^2]}{E[(\boldsymbol{y} - \mu)^2]} \cdot 100 \tag{48}$$

Table 5.1: Period of time series used to predict the tide, the GOF of the tidal model to the tide gauge measurements at Talcahuano, Corral and Valparaiso.

Station name	Period time series	GOF [%]	RMSE [cm]	Number of constituents
Talcahuano	30/11/09-26/02/10	98.8	4.8	35
Corral	30/11/09-30/01/10	96.8	10.9	34
Valparaiso	30/11/09-26/02/10	96.6	4.9	35

Table 5.1 shows that a different period is used to predict the tide during the tsunami at station Corral. This is due to an inconsistency in the measurements between the month February and the previous months. This particular period is chosen because it results in a higher GOF and a smaller root-mean-square (RMSE) of the residuals:

$$RMSE = \sqrt{\frac{1}{N}\sum_{i=1}^{N} |\, \boldsymbol{y}_i - A\mathbf{x}\,|^2} \tag{49}$$

The tidal prediction is calculated with Equation (29) for a period ranging from one day prior to the tsunami till the end of the tsunami simulation. The RMSE of the tidal prediction for Corral using the same period of observation as chosen for Talcahuano and Valparaiso is 23.4 cm. Using only the month of February for the prediction resulted in a RMSE of 14.0 cm. The question remains whether a RMSE of 10.9 cm over a tidal amplitude of approximately 80 cm is acceptable. We expect that an error of 10.9 cm is small enough to compare the observations against the tsunami simulation results, as the tsunami amplitude at Corral is approximately 2.6 m. The tidal prediction resulting from the tidal fit is illustrated in Figure 5.2. This figure shows that the tidal prediction fits the observation well and that the tsunami's peak to peak amplitude is much bigger than the tidal amplitude.

Another point of discussion is the number of constituents used to predict the tidal signal. The tidal model contains more than 34 tidal constituents to achieve a GOF larger than 95%. The table in Appendix B shows that the amplitude of many constituents is very small. It is expected that only the

tidal constituents with diurnal period and semi-diurnal have a significant effect on the water level during the tsunami. However, due the small effort to fit all constituents, it is chosen to use all constituents with the aim to achieve a higher fit for the tidal prediction.

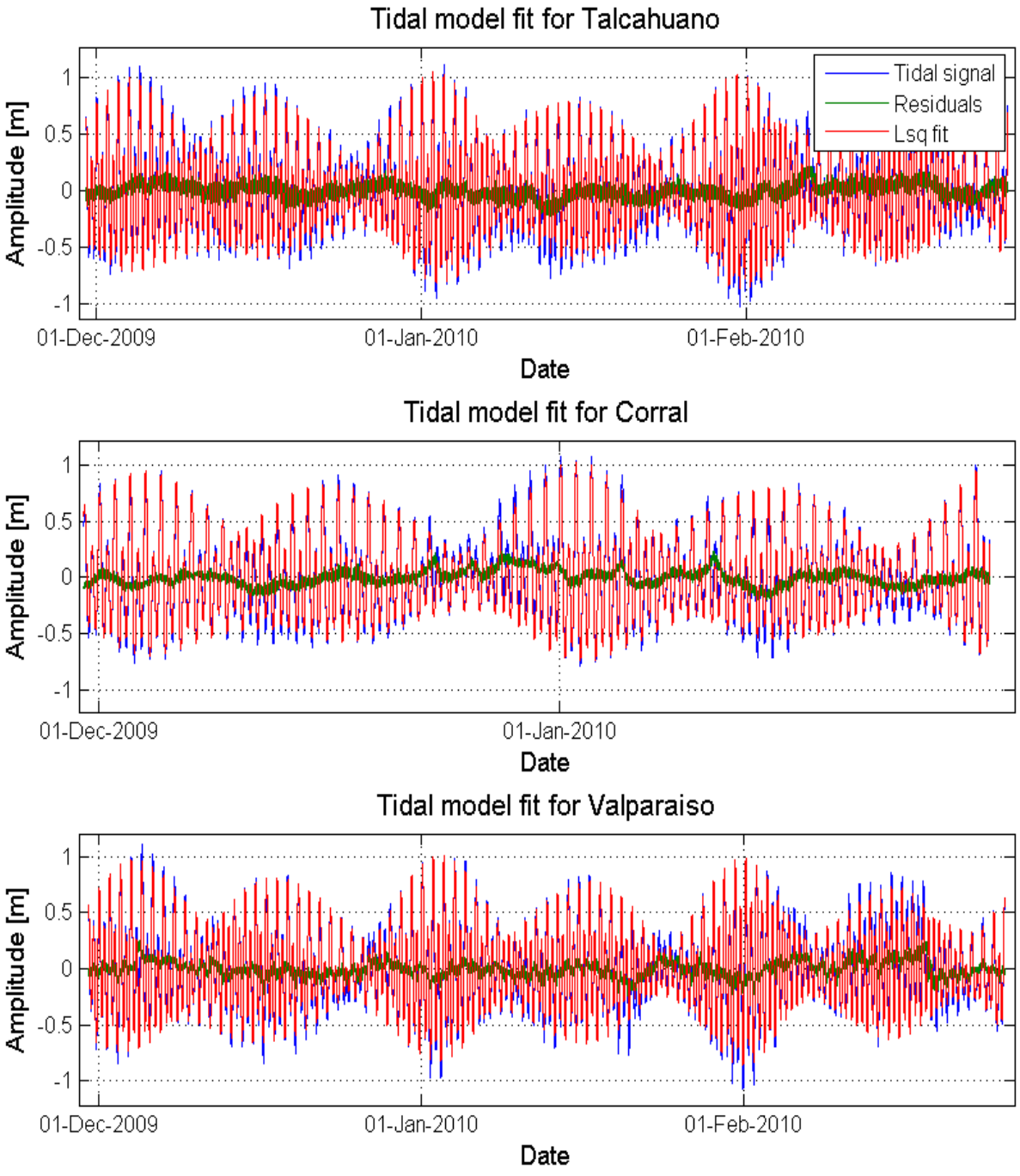

Figure 5.1: Tidal model fit to the observation of normalized sea surface level at Talcahuano, Corral and Valparaiso tide gauge using a Matlab based tidal fit toolbox of Aslak Grinsted.

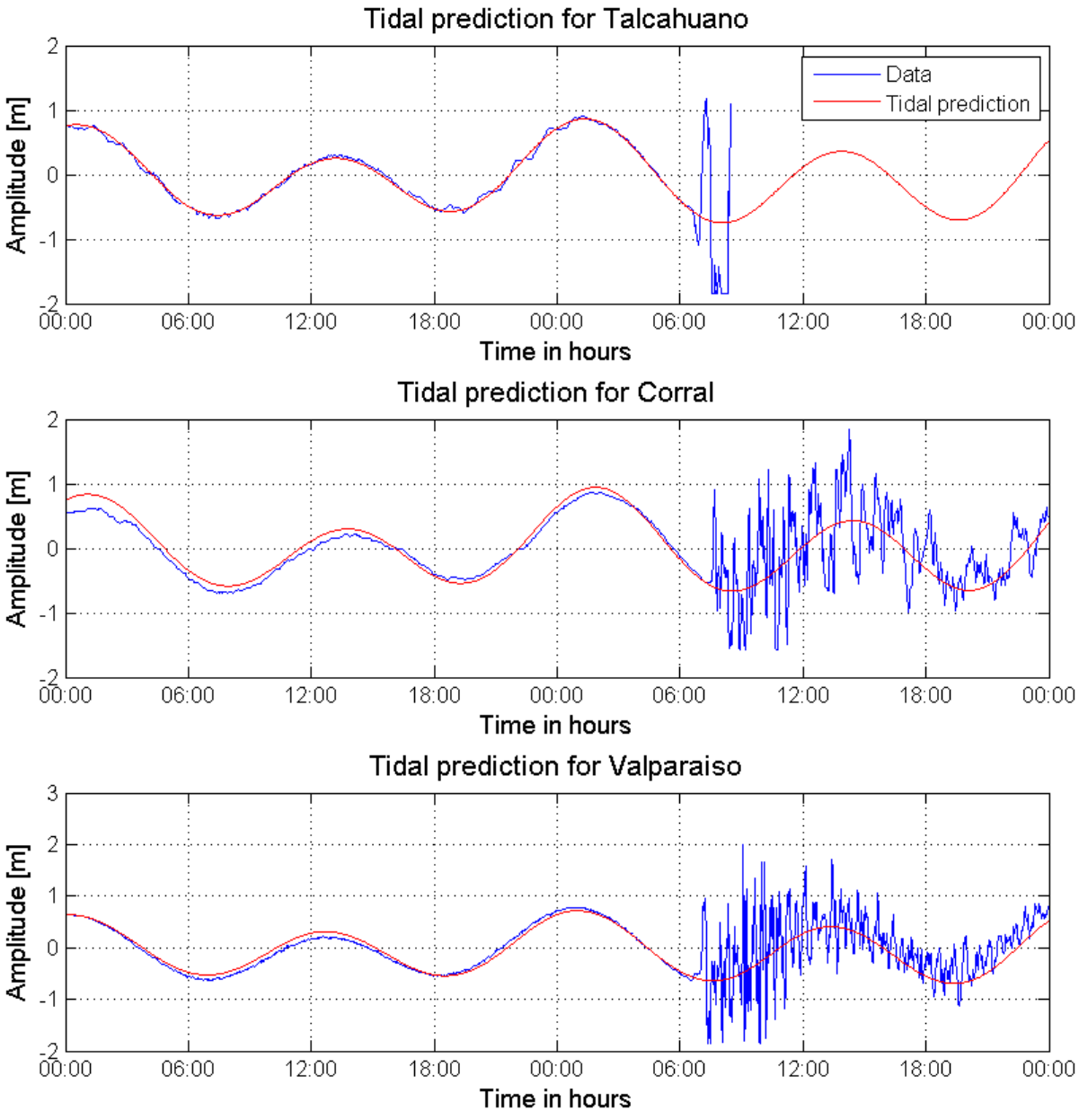

Figure 5.2: Tidal prediction for stations Talcahuano, Corral and Valparaiso. Prediction starts from 26-02-2010 00:00 till 28-02-2010 00:00.

5.2. Model validation at tide gauges

In this paragraph we will discuss the simulation results at the tide gauge stations Talcahuano, Valparaiso and Corral. The simulation results obtained by different source models will be compared to tide gauge observation at these stations. Subsequently spatial variation in the wave field will be discussed with the aid of spectral analysis of surface elevation. We start this discussion by interpreting the results at the former station.

5.2.1. Tsunami impact at tide gauges

The 2010 Chilean Tsunami is simulated with three different source models describing the vertical uplift and subsidence of the ocean floor that occurred during the earthquake. The simulation results and tide gauge observations are visualised in Figure 5.3. The outstanding feature of the surface-elevation observations at Talcahuano is the discontinuity in surface elevation 1 hour after the earthquake. The discontinuity is a consequence of the relatively shallow water-depth of approximately 2 meters at the location of the tide gauge. The figure indicates that the modelled wave amplitude is larger than the water-depth. This implies that the pressure gauge gets exposed several times when the water retreats. During these exposures no measurements are taken. This ambiguity is not a consequence of the discretisation scheme or the model's accuracy but it is rather related to the resolution of the mesh used. The maximum resolution of the generated mesh and bathymetry is 80 m. Moreover, the location of the water level output of the model does not coincide with the mesh-node where the water level is computed. Therefore the model uses linear interpolation to calculate the water elevation at the observation sites. The interpolated water level is thus based on the enclosed triangle, this causes the modelled wave trough to be bigger than the actual water depth. Another interesting point of the surface-elevation observation is that the recording stops suddenly when the second wave arrives at this location. It was assumed that that the tide gauge was damaged by the destructive tsunami wave 2.

According to the tide gauge observation the initial tsunami wave arrived 27 minutes after the initial earthquake shock at Talcahuano harbour. However, the simulations presented here, based on Moreno's and Vigny's earthquake solution, in Figure 5.3 and Figure 5.4 show that the arrival time of the first wave is approximately 24 minutes after the earthquake. The difference between the tide gauge data and the model results is due to the assumption that the earthquake rupture is established instantaneously. According to the USGS (2010) the duration of the rupture process of the earthquake lasted for approximately 3 minutes. Moreover the rupture propagation along the fault might also have an impact on the generated tsunami. This explains to a large extent the offset observed between the modelled results and the tide gauge data.

Before the wave arrived a slight drop in water level is measured at the tide gauge. This drop is a consequence of a wave trough generated in the subsidence area of the earthquake. This drop is captured best when modelling the tsunami with Moreno's source model. In contrast to this a large difference is observed between the tide gauge data and model results when using the Delouis source model. The resulting surface elevation is initially 1 meter according to Delouis' solution. This is unlikely to be accurate as the tide gauge observations and other model results contradict this. The difference between Delouis' source model and those of Moreno & Vigny is the location of the seismic asperity relative to the trench. The Delouis' rupture area was much closer to the coast than the latter, see Figure 3.3. The consequence is that the vertical uplift at Talcahuano harbour is overestimated by the former source model. The Delouis source model however also shows the drop in water level prior to the first tsunami wave.

Figure 5.3 shows that the initial tsunami wave is certainly not the biggest. This interesting feature, which is of great importance for this research, is captured by all source models, even the Delouis model. This wave is unfortunately not recorded by the tide gauge but is supported by the results of survey campaigns of the ITST (Fritz, et al., 2010). The ITST deduced the wave height from bleached

algae, waterlines and run-up. The wave height is 4.5 m, 5 m and 6 meters in height according to Delouis's , Vigny's and Moreno's simulation results respectively. In the paper by Fritz, et al (2010) it is stated that the wave height was between 4.7 m and 6.7 m.

Another notable similarity between the source models is that all of them produce the same number of waves with wave crests occurring at approximately 2, 2.5, 3 and 3.5 hours after the earthquake rupture. For convenience the power spectrum of the wave field has been computed and visualised to highlight this characteristic of the wave field. The wave field which is visualised in Figure 5.3. shows that all source models predict a spectrum with distinct peaks at wave periods of approximately 35 and 93 minutes. It is notable that the 3 source models all produce the same wave spectrum, despite their significant differences, see Figure 3.3. It can be concluded that the wave field is a function of the bathymetry rather than the significant differences in the available source models.

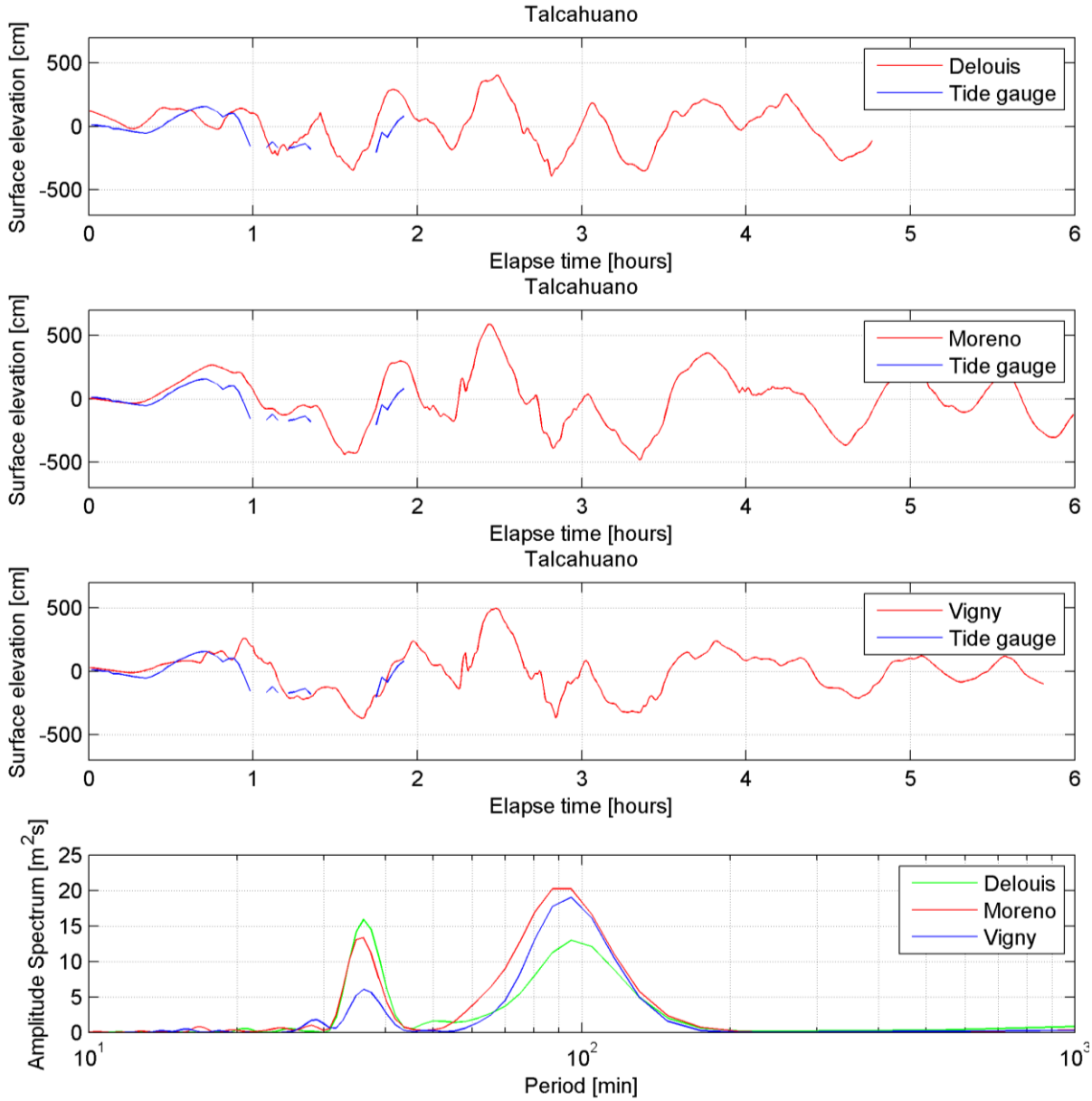

Figure 5.3: Validation of the model results against tide gauge at Talcahuano bay. Delouis' time series is shorter because the simulation got "killed" due to external reasons regarding the cluster protocols. The amplitude spectrum of Delouis, Moreno and Vigny are determined with the same number of data point.

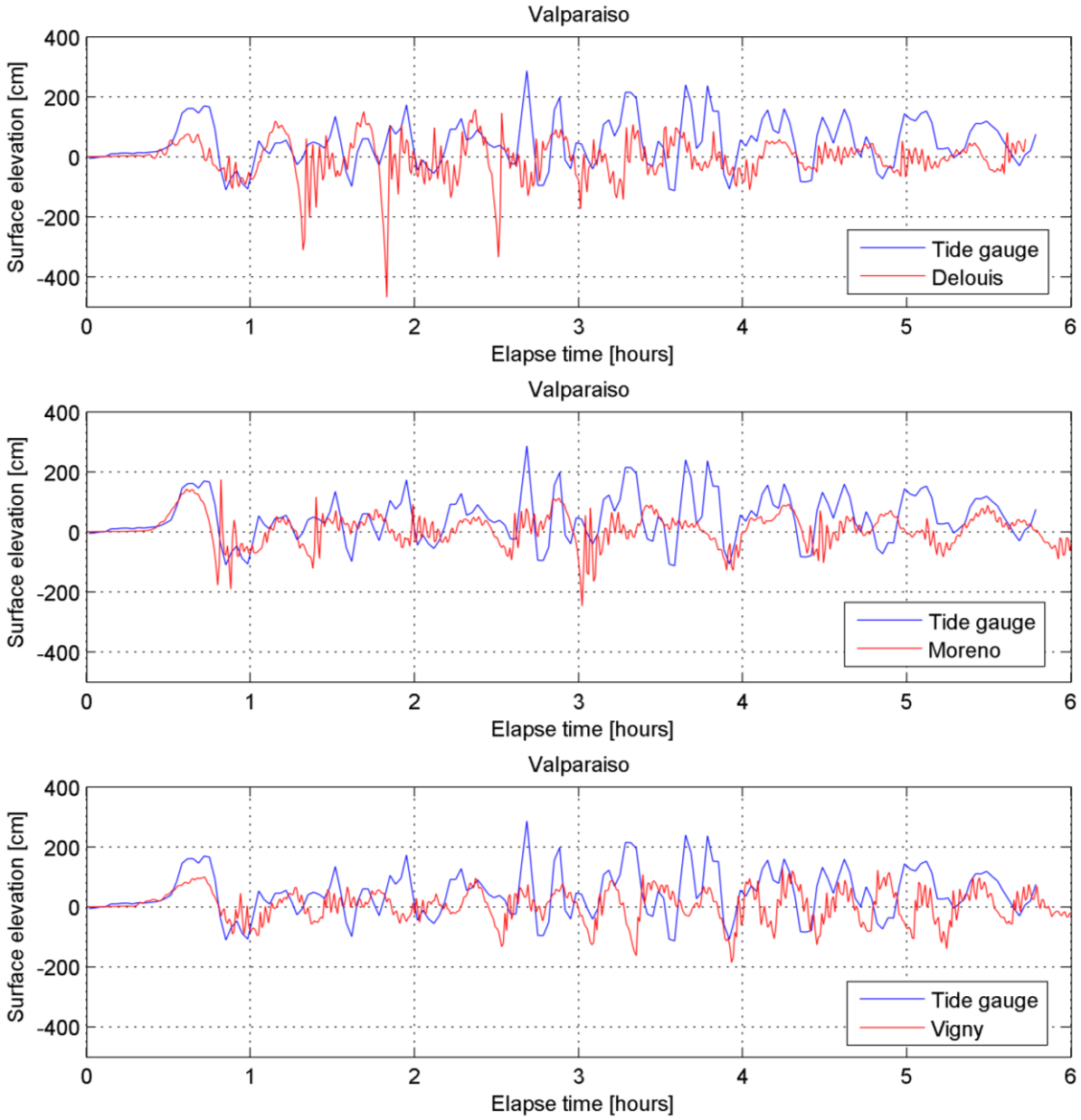

Figure 5.4: Validation of the model results against tide gauge in Valparaiso.

Unlike the observations at Talcahuano the observations at Valparaiso and Corral are continuous and cover the entire event. A difference with the modelled results between Talcahuano and Corral is that the model (using Vigny's and Delouis' solution), compared to observations, clearly underestimates the wave amplitude of the first wave. The model fit at these locations is much worse than at Talcahuano. The modelled surface elevation is in fact at several epochs even out of phase with the observations i.e. a wave trough is modelled while the tide gauge observes a wave cres. The reason for the bad fit could be subscribed to the resolution of the bathymetry. At Talcahuano, the GEBCO bathymetry data set has been improved with several nautical charts from the Chilean navy to get a resolution up to 80 m. The available bathymetry dataset at Valparaiso and Corral is only based on the GEBCO database which has a resolution of approximately 1 000 m. The coarse bathymetry (and mesh) limits dramatically the accuracy in simulating the tsunami propagation in coastal regions. The model can't capture all of the details of the wave reflections, refraction and diffraction from small scale features in the bathymetry and topography (real world) which are not present in the coarse bathymetry data.

The highest wave are approximately 2.6 m and 1.5 m above MSL at Valparaiso and Corral respectively. This is, in contrast to the modelled wave height of 6 m at Talcahuano, quite small. This is obviously related to the location of the observation site. Talcahuano is just 100 km from the earthquake's epicentre. Valparaiso and Corral are relatively far from the epicentre and outside tsunami's near field region, the region of significant vertical deformation. The modelled sea surface oscillations at Valparaiso and Corral, see Figure 5.4 and Figure 5.5, show a faster sea surface oscillation envelope than the oscillation observed at Talcahuano Figure 5.3. This interesting feature will be discussed with the aid of spectral analysis in Chapter 6.3.

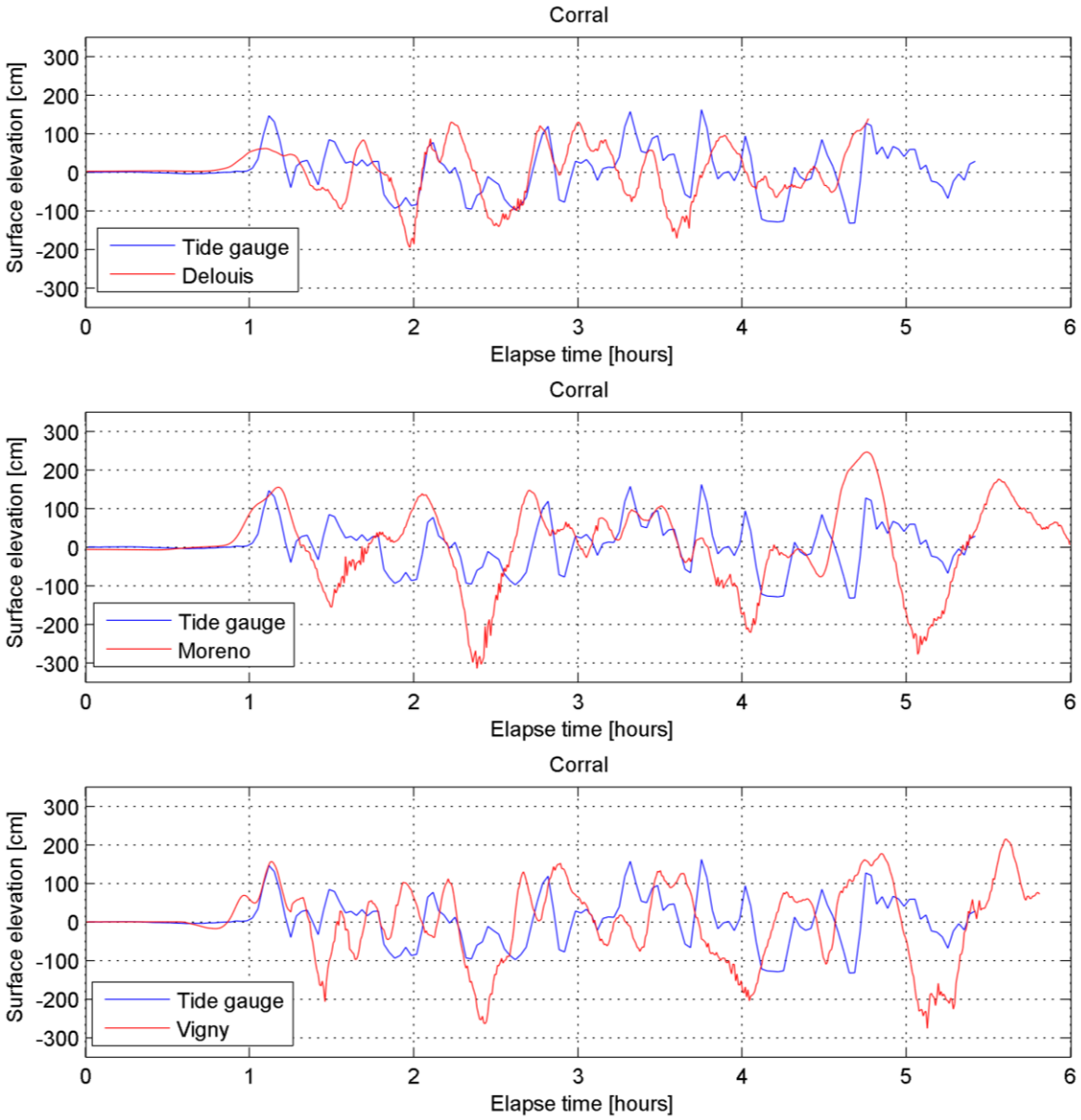

Figure 5.5: Validation of the model results against tide gauge in Corral

5.3. Validation of model results in the far field

The generated tsunami is observed at several locations across the Pacific. The observations and modelled tsunami results support the widely known characteristic that tsunami waves retain their energy for thousands of kilometres. Significant tsunami signals were recorded by four different DART buoys, namely 32412, 32411, 51406 and 43412, shown in Figure 4.1. Validation of model parameters is the main purpose for simulating the model in the far field. Moreover simulation results in the far field are better suited to distinguish between the available source models because their location in the deep ocean minimises the error related to reflection of tsunami waves at the continental margins.

5.3.1. Tsunami signal at DART buoys

The simulation results obtained using the different source models has been compared against the observations at DART buoy locations. The maximum resolution of the Pacific wide mesh in the deep ocean is 14 km. This implies that the mesh node location doesn't coincide with the Dart location. Therefore a linear interpolation method has been applied to obtain the surface elevation at the DART buoy locations.

The computed surface elevation time series for DART 32412 has been plotted and visualized in Figure 5.6. The blue line indicates the filtered DART buoy observations and the red line denotes the modelled surface elevation. The tsunami signal in the far field is characterised by distinct peaks implying a wave front followed by a wave-train. The initial wave is a result of the leading tsunami wave crest that propagated from the source region. It arrived directly and did not reflect from the coast. The rest of the wave-trains are however due to by leaky edge waves and wave reflections from the islands in the Pacific Ocean (Yamazaki & Cheung, 2011). The magnitude of the wave front is also several times higher than that of the wave train. This is reasonable, as the wave energy dissipates significantly after reflection.

The recording at DART 32412 also recorded the seismic wave generated by the earthquake (NOAA, 2010). The seismic wave is obviously much faster than the tsunami wave. The arrival times of the seismic wave and the tsunami wave are 7 minutes versus 3 hours respectively. This corresponds to a seismic wave velocity of 5.5 km/s and a tsunami wave celerity of 0.2 km/s (800 km/h). Please note the observations from DART 32412 are high-pass filtered instead of band-pass to preserve the seismic wave in the signal.

In contrast with the tide gauges the model fit is very good at the DART buoys. This indicates the robustness of H_2Ocean tsunami model. The model is able to predict (modest) tsunami amplitudes even though the stations are located up to 6700 km away from the source, and for simulation times larger than 10 hours. The problem with tide gauges is that their location is characterized by relatively shallow water. Thus every discontinuity in the topography has a significant effect on the wave propagation. These small scale features are not represented by the coarse bathymetry dataset resulting in the poor accuracy of the model results. This problem manifests itself also in the far field data. Even though the model predicts the initial tsunami wave very accurately it is notable that the prediction of the wave train is at some points rather bad. The short waves are a result of reflection from several islands and different parts of continental margin of South-America. The poor resolution of the coastline, bathymetry at coast and the initial field used results in the less accurate prediction observed in the wave train.

The difference between the results using Delouis, Moreno and Vigny as initial field is rather modest. The results obtained using Delouis' solution for the vertical uplift underestimates the wave front while Moreno's solution result in a slight overshooting. The location of Delouis' initial field is relative close to the coast. This implies that the DART buoy is slightly further away from the modelled epicenter for Delouis' solution than for Moreno's solution. This might explain why Delouis' solution underestimates the height of the initial tsunami wave and resulting wave train at the DART buoys.

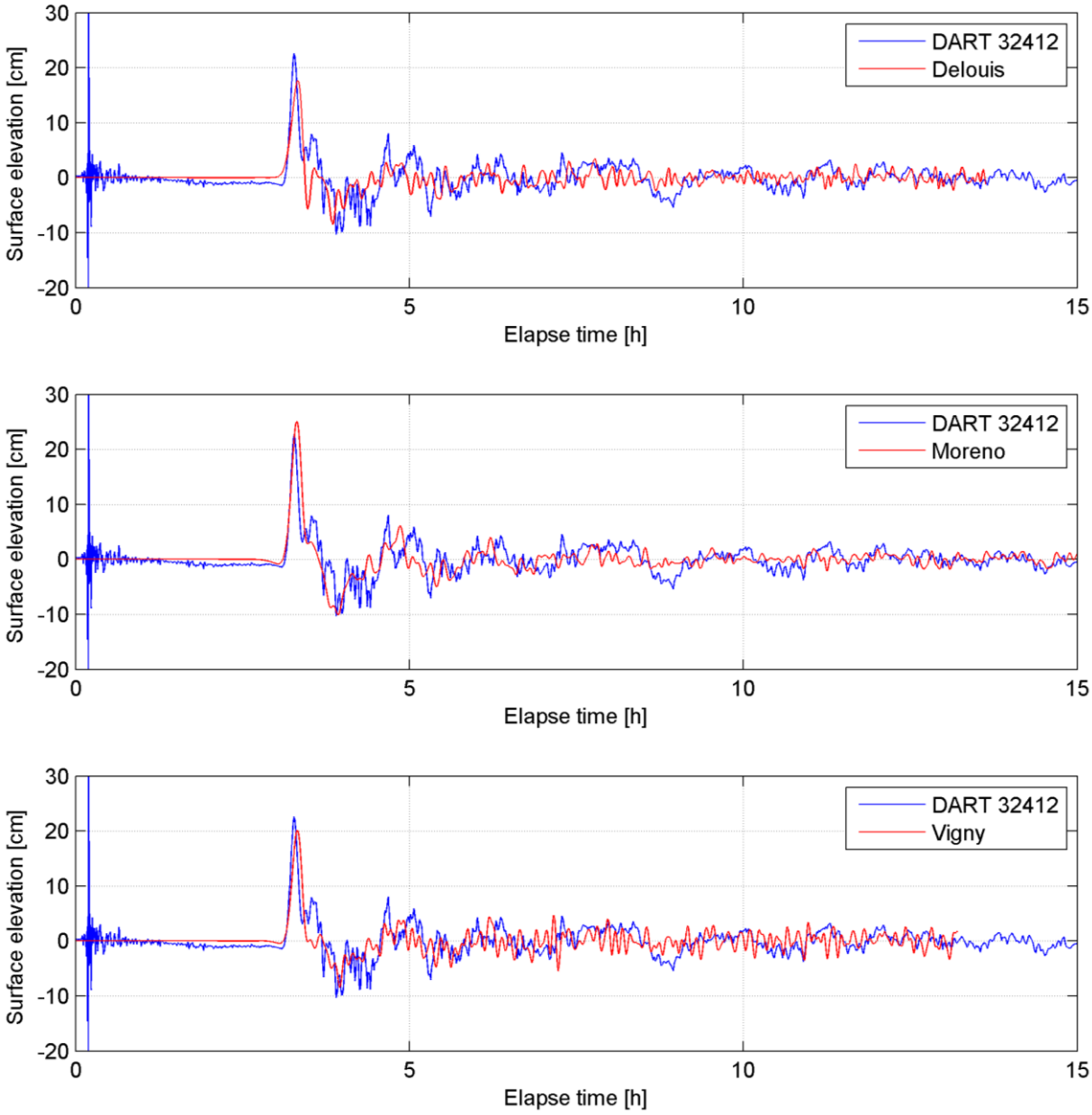

Figure 5.6: Validation of model results, according to initial fields by Delouis, Moreno and Vigny against DART 32412

The signal observed at DART 32411 (Figure 5.7) differs from the tsunami signal observed at the other DART stations. The signal at this station doesn't contain the distinct initial wave observed at the other stations. The height of initial wave in this signal is rather modest and in the same order of magnitude as the successive oscillations. The reason for this is that this station is located outside the main energy arc of the tsunami (Yamazaki & Cheung, 2011). Figure 4.1 shows the location of the DART stations in the Pacific Ocean. DART 32411 is located just behind the Galápagos islands. The Galápagos' coastal margin is characterised by a steep insular slope which modulates the signal at DART 32411 through refraction and diffraction (Chandrasekera & Cheung, 2001). The reason that the tsunami arrived distorted through refraction and diffraction explains also to a large extent the poor fit. The bathymetry data set doesn't capture all of the features of Galápagos' coast, this results in less accurate wave prediction.

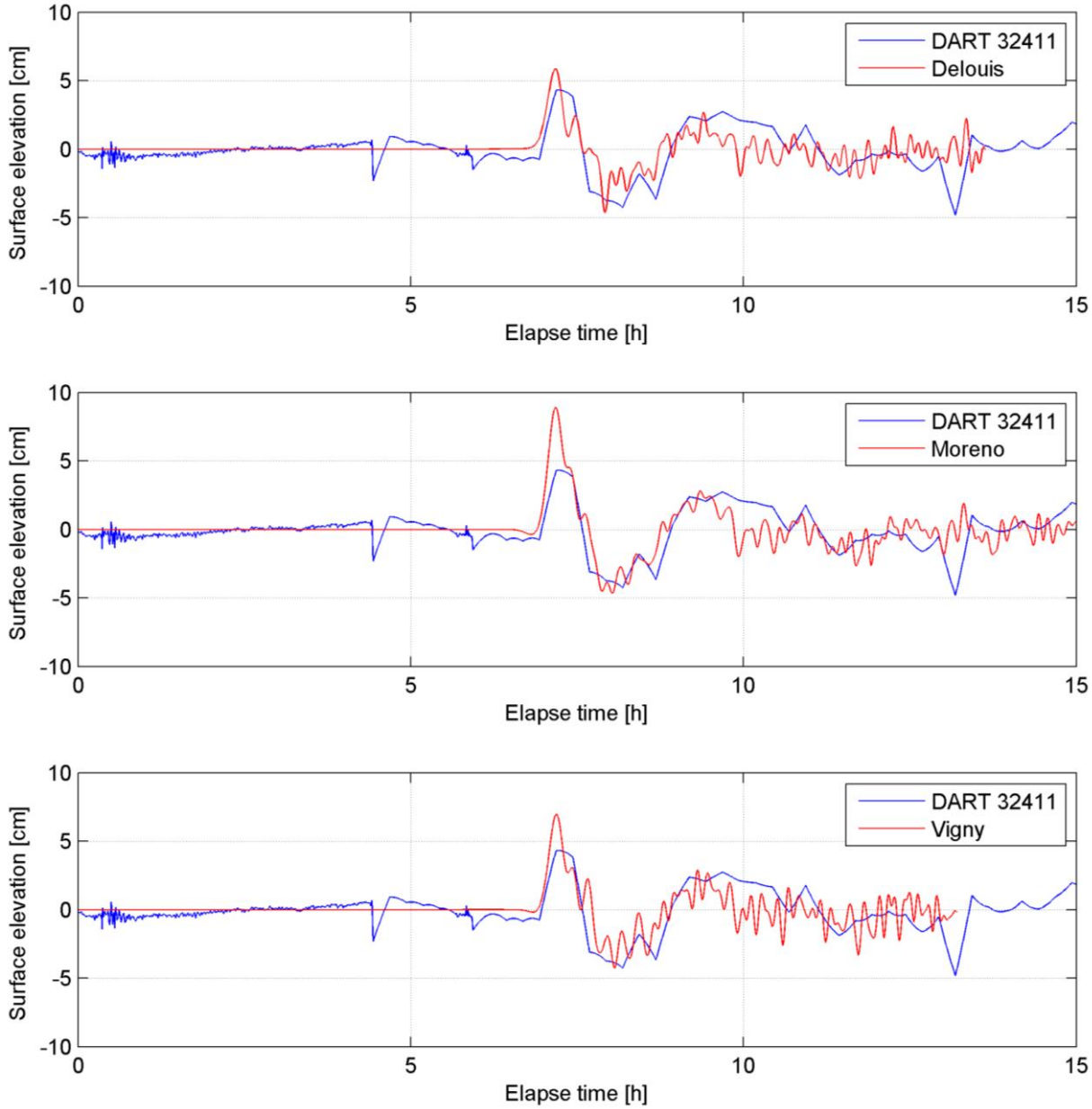

Figure 5.7: Validation of model results, according to initial fields by Delouis, Moreno and Vigny against DART 32411

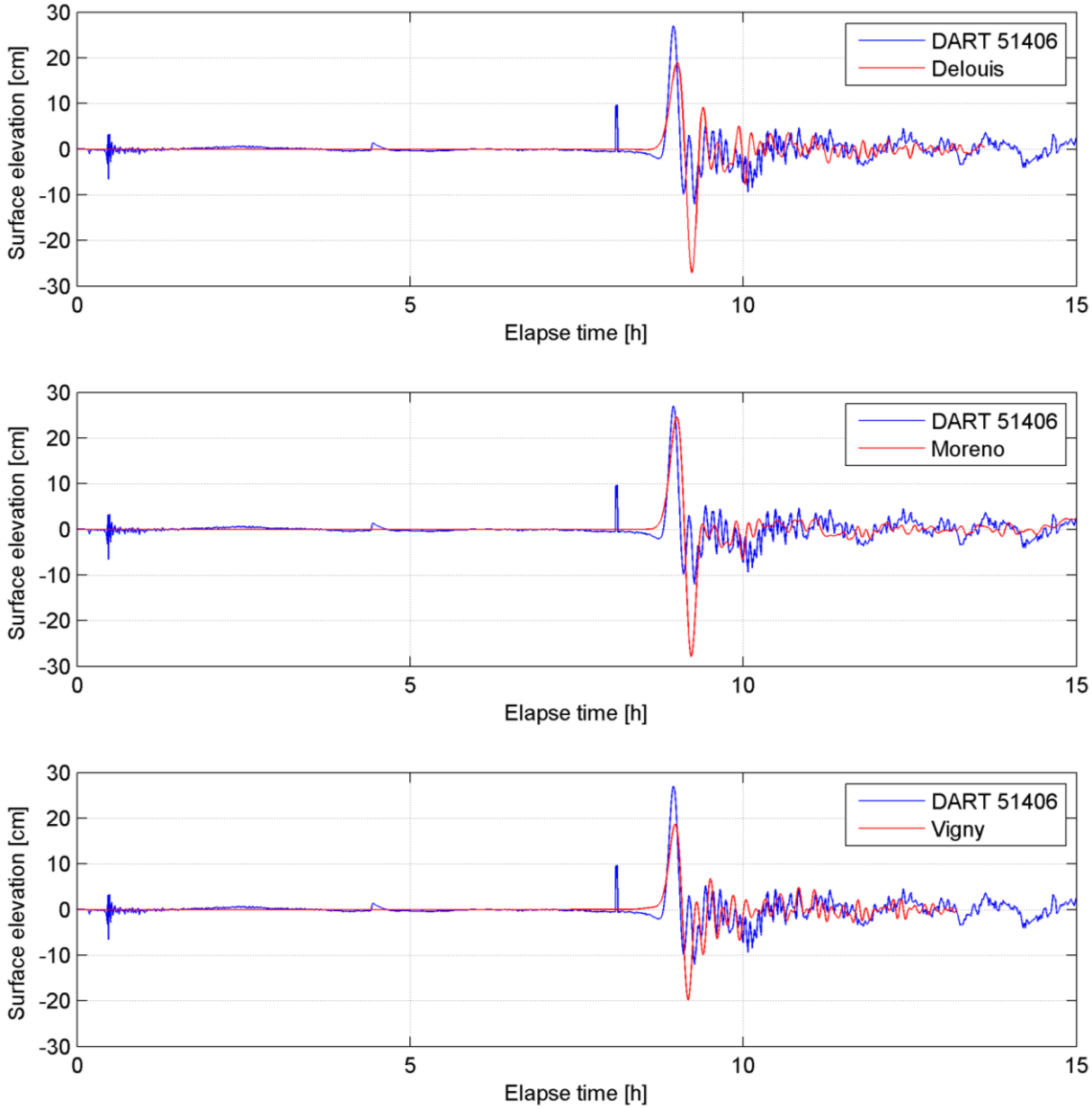

Figure 5.8: Validation of model results, according to initial fields by Delouis, Moreno and Vigny against DART 51406

Shallow water waves retain their energy for long distances in deep water (Vreugdenhil, 1994). This characteristic of long waves is also highlighted in the observation and model results at all DART buoys across the Pacific. The wave height of the tsunami wave front at the closest DART buoy is approximately 24 cm. The height of this wave at DART 51406 and 43412 is about 25 cm and 12 cm respectively at a distance of 6100 and 6700 km from the epicentre. The fact that the DART 51406 is located in the main energy arc of the tsunami is the reason for the high wave height. The arrival times at these two stations is 8.5 and 9.5 hours respectively. This corresponds with average tsunami wave speed of approximately 720 km/h and 705 km/h respectively. The average depth of Pacific Ocean is 4280 m (Encyclopaedia Britannica Inc., 2006). The wave velocity of tsunamis is according to the shallow water theory proportional to the water depth:

$$c = \sqrt{gh} \tag{50}$$

The velocity corresponding with $h = 4280$ is 737 km/h. This is indeed in the same order of magnitude as the average velocity resulting from the tsunami arrival times at the DART buoys. So the

model results and observations confirm the validity of the relation between propagation speed and water depth (50).

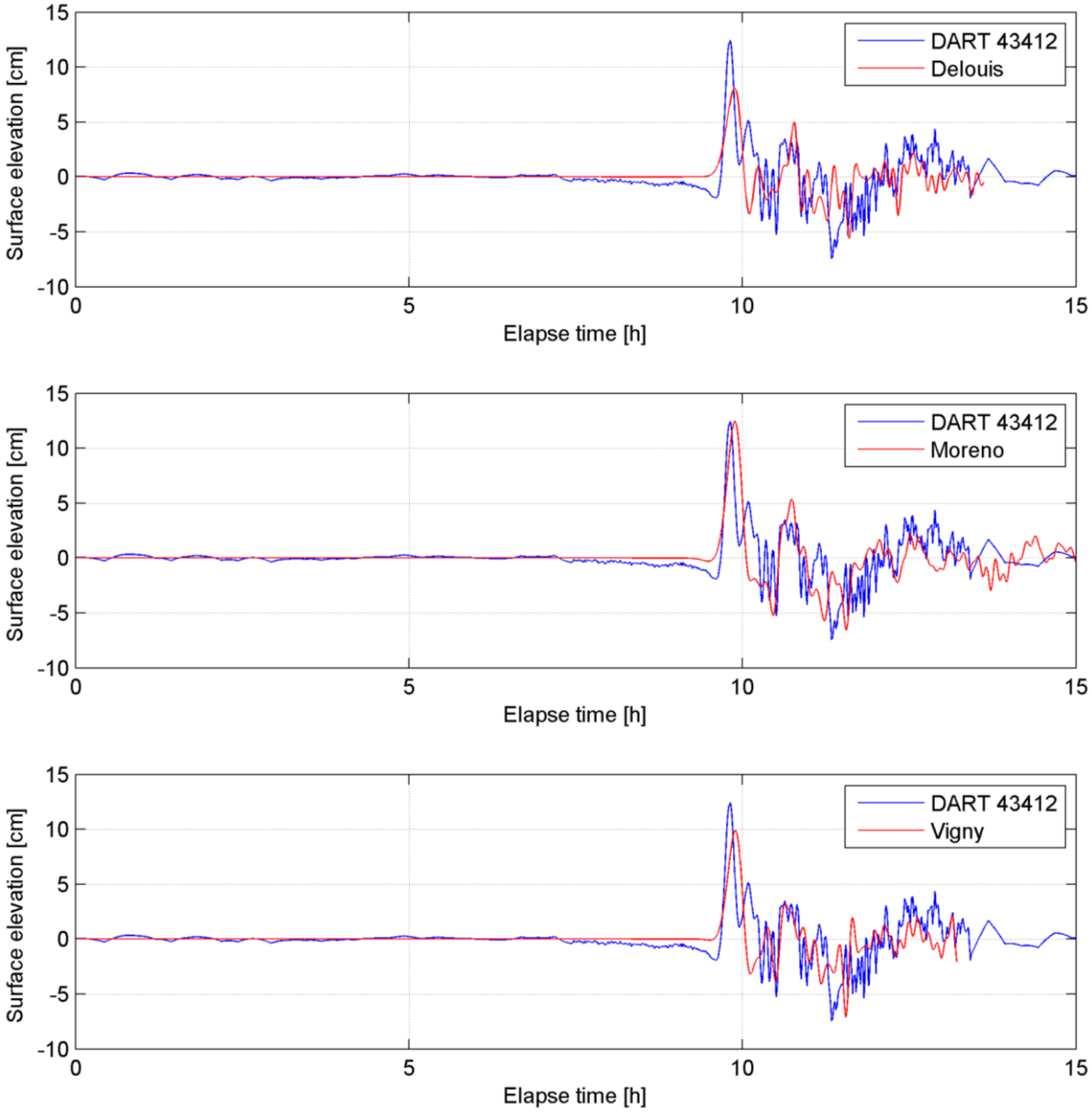

Figure 5.9: Validation of model results, according to initial fields by Delouis, Moreno and Vigny against DART 43412

5.4. Model selection

In previous paragraph model results were presented and discussed. The main emphasis of this paragraph is to discuss, in a more quantitative sense, the quality of the fit of the tsunami signal generated by the available source models. The aim is to compare the model error i.e. misfit, of the tsunami simulation according to the available source model, by the test statistic defined in Chapter 4.3:

$$\underline{T}_{q=m-n} = \frac{\hat{\underline{e}}^T Q_y^{-1} \hat{\underline{e}}}{m-n} \tag{51}$$

The value of this property has been computed for each simulation at all observation stations and has been summarized in Table 5.2. The table also includes the value of the critical value which discriminate whether the null hypothesis is valid or should be rejected. A significance level $\alpha = 0.05$ is taken which implies that the probability that the fit between the observed and modelled signal arose by chance is smaller than 5%.

Table 5.2: The calculated test statistic at different observation stations and $k_{\alpha=0.05}$ denotes the critical value of the test statistic.

Station name	Delouis	Moreno	Vigny	$k_{\alpha=0.05}$
DART 32412	0.999	0.998	0.998	1.042
DART 51406	0.999	0.999	0.998	1.042
DART 32411	0.991	0.993	0.992	1.042
DART 43412	0.996	0.996	0.996	1.042
Talcahuano	1.345	1.296	1.999	1.324
Valparaiso	0.761	1.049	1.010	1.197
Corral	1.157	1.034	0.948	1.197

The test statistic calculated for each earthquake solution indicates that all source models produce realistic tsunami signals at the observation sites. The differences in accuracy are in general quite small except for the tide gauge at Talcahuano harbour. The tsunami signal generated by the Delouis' source model does not fit the data very well. This is likely due to the uplift being located to close to Talcahuano, see Figure 3.3. The rejection of the Vigny model was not expected because the initial wave and timing are reproduced better than Moreno as indicated by Figure 5.3. We expected that due to the second peak predicted by Vigny causes rejection of the hypothesis. We therefore only consider the Moreno source model in the following chapter.

6. Results at regional scale

This chapter explores the propagation and evolution of the Chilean Tsunami using the initial source model described by Moreno et al. (2007). The bathymetry has a major impact on the evolution of the edge waves therefore in the first section we consider the bathymetry. In the following section a discussion is presented of the evolution of the tsunami and its regional impact. Finally we also consider the evolution of the tsunami wave and the role of edge waves in this chapter.

6.1. Bathymetry at regional scale

In Figure 6.1 the GEBCO 30'' dataset has been visualized at regional scale. In this figure (left) the 1000 m, 500 m and 200 m depth contours are highlighted in black, yellow and red respectively. The 1000m depth contour is pretty close to the coast implying that the domain has a relative large depth, reaching maximum values above 6 000 m located between 50 km and 120 km from the coast. Another interesting bathymetric characteristic highlighted by the contours is the relatively narrow continental slope. The (longitudinal) gradient of this slope was also calculated as a function of latitude:

$$\left(\frac{\partial z}{\partial x}\right)_j = \frac{\Delta(z_i - z_{i+1})}{\Delta(x_i - x_{i+1})} \tag{52}$$

where z and x are the depth and the longitudinal-position of the i^{th} - contour with $i = 1,..,4$ representing the depth contours of 1000 m, 500 m, 200 m and shoreline respectively. Furthermore, $j \in [32°S, 40°S]$ denotes the latitudinal-index. The resulting gradients have been plotted on logarithmic-scale (right).

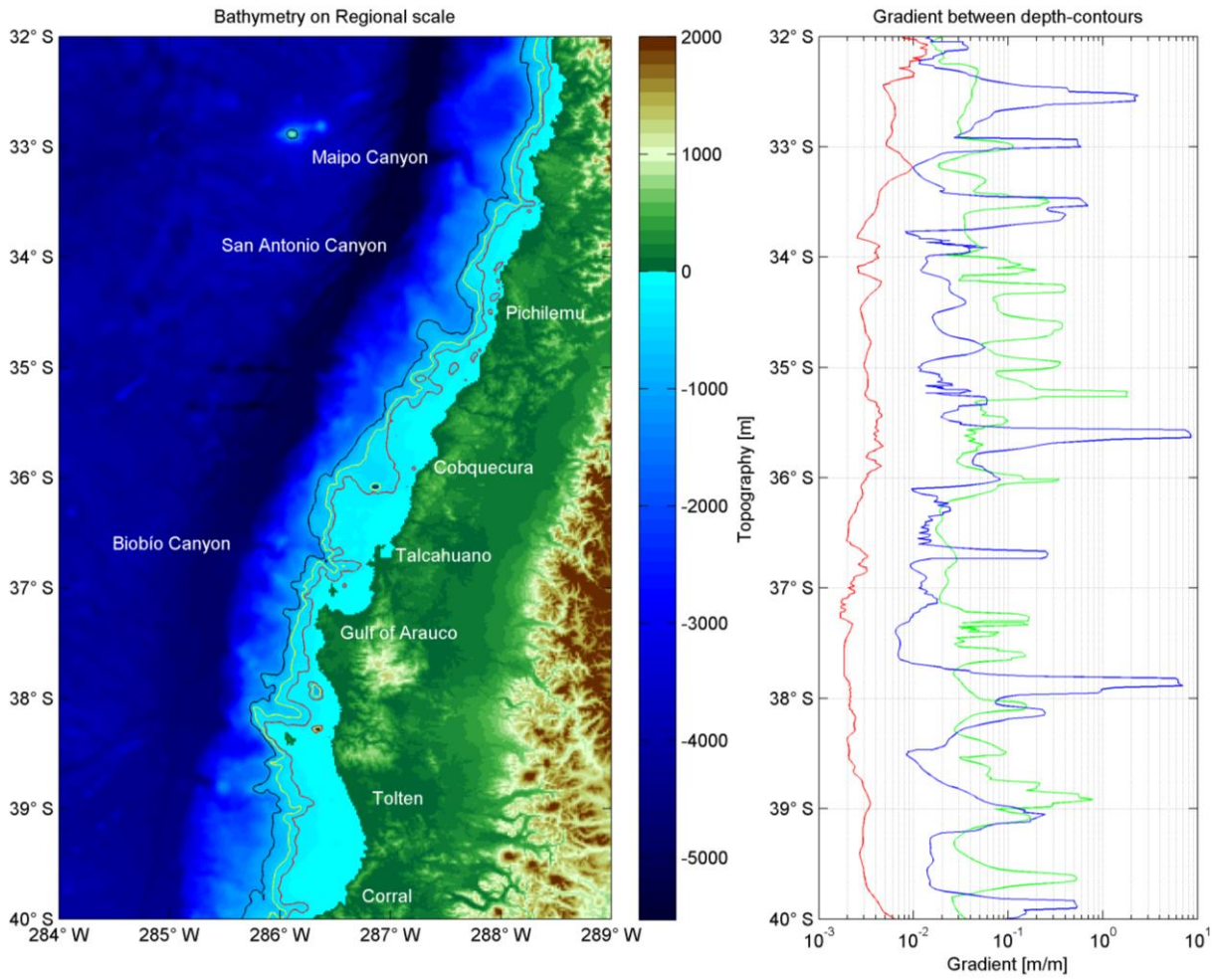

Figure 6.1: (Left) Bathymetry at regional scale highlighting the submarine canyons and the 1000 m, 500 m and 200m depth contour indicated by the black, yellow and red contours respectively. (Right) Gradient in latitudinal direction between 1000 m and 500 m depth contour (green), 500 m and 200 m depth contour (blue) and 200m depth contour and the shoreline (red).

These results highlight that the Chilean bathymetry is characterised by a very steep continental slope. The narrow continental slope however is followed by a gentle sloping continental shelf. The figure shows that the order of magnitude of the continental shelf is approximately one order of magnitude smaller than the gradient of the continental slope.

The gradient of the continental shelf is also much smoother in the alongshore direction than the gradient of the continental slope. This implies that the gentle continental shelf is relatively uniform in the alongshore direction. Starting from the north we see that the continental shelf is quite narrow until south of the submarine canyon in the continental slope at Pichilemu, with average slope $\beta = 0.006$. The steepness in this region reaches its maximum in the far north and upstream of the Maipo submarine canyon. The order of magnitude of the slope at these two locations is of the same order of magnitude as the continental slope. Between Pichilemu and Talcahuano there is a distinct average slope $\beta = 0.045$. In this region two distinct peaks are visible, the first indicating the canyon south of Cobquecura and the second the canyon south of Talcahuano indicating the Biobío (submarine river) Canyon. South of the Gulf of Arauco we see a wide continental slope $\beta = 0.001$ which increases rapidly to a slope $\beta = 0.005$ south of Corral. It should be noted that the gradient of the slope in Equation (1) the evolution of edge waves.

6.2. Tsunami impact

Figure 6.2 shows snapshots of the tsunami simulation using Moreno's earthquake source model. Panel a shows the initial state which represents the vertical uplift by the earthquake rupture. The second panel (b) shows the wave spreading 12 minutes after the earthquake rupture. The initial wave propagation is as expected in Figure 6.2b, with the uplift and subsidence propagating away from the source region in Figure 6.2b. The intense red color near the coast in Figure 6.2 b and c shows the increase in wave amplitude as the tsunami floods the coast. In Figure 6.2 c we also begin to see the distinct patches of higher (red) and lower (blue) amplitudes emerging along the entire coast. This apparent wave trapping along the Chilean coast is a distinct feature of Figure 6.2 c-f.

A point of interest is the leading wave trough indicated by the blue colour in Figure 6.2b. It is expected that this wave is generated by the area of subsidence along the coast of Chile, which caused the drop in the surface elevation at the Talcahuano tide gauge station (see Panel a Figure 6.3). Another interesting point is that the wave speed in the seaward direction is much faster than in the shoreward direction. This is expected as the wave speed is proportional to depth. This fact is also underlined in panels c and d.

Tide gauge observations show that the tsunami arrival at Valparaiso is approximately 2 minutes earlier than Talcahuano, compare Figure 5.3 and Figure 5.4. This could be explained by the fact that the water depth is larger for the northern part of this region (Figure 6.1) which results in higher wave speed and shorter arrival times. Moreover, the Talcahuano tide gauge is located in a sheltered area in the bay of Concepción where the water depth is relatively shallow (Figure 6.3 and Figure 3.1). This explains why the tsunami is detected later in Talcahuano than in Valparaiso.

The reason that the wave arrived much later in Corral (panel d) is that it is located farther away from the source region. The leading wave to arrive in Corral comes from the patch of uplift at the southern limit of the source model in Figure 3.3, see also in Figure 6.2 a. In addition the water depth is shallower in the southern part of the simulation domain. Thereby, Corral is located in the far field where the leading wave is a consequence of the minor tsunami wave direction through diffraction which is the "turning" of waves towards areas with lower amplitudes due to amplitude changes along the wave crest (Holthuijsen, 2007).

Finally, a persistent wave oscillation is depicted in the last two panels, Figure 6.2 e-f. Even three hours after the rupture the surface elevations are of the same order of magnitude as the initial wave. However, the significant wave activity after 3 hours is much more confined to the coast. A characteristic of trapped edge waves is that their wave energy decays slowly as they propagate over the continental margin (Rabinovich, Stephenson, & Thomson, 2006). We speculate that the presence of significant wave activity after several hours, highlighted in Figure 6.2 e and f, was associated with trapped edge waves. The presence of edge waves will be explored further with the aid of the energy flux quantity in the last section of this chapter.

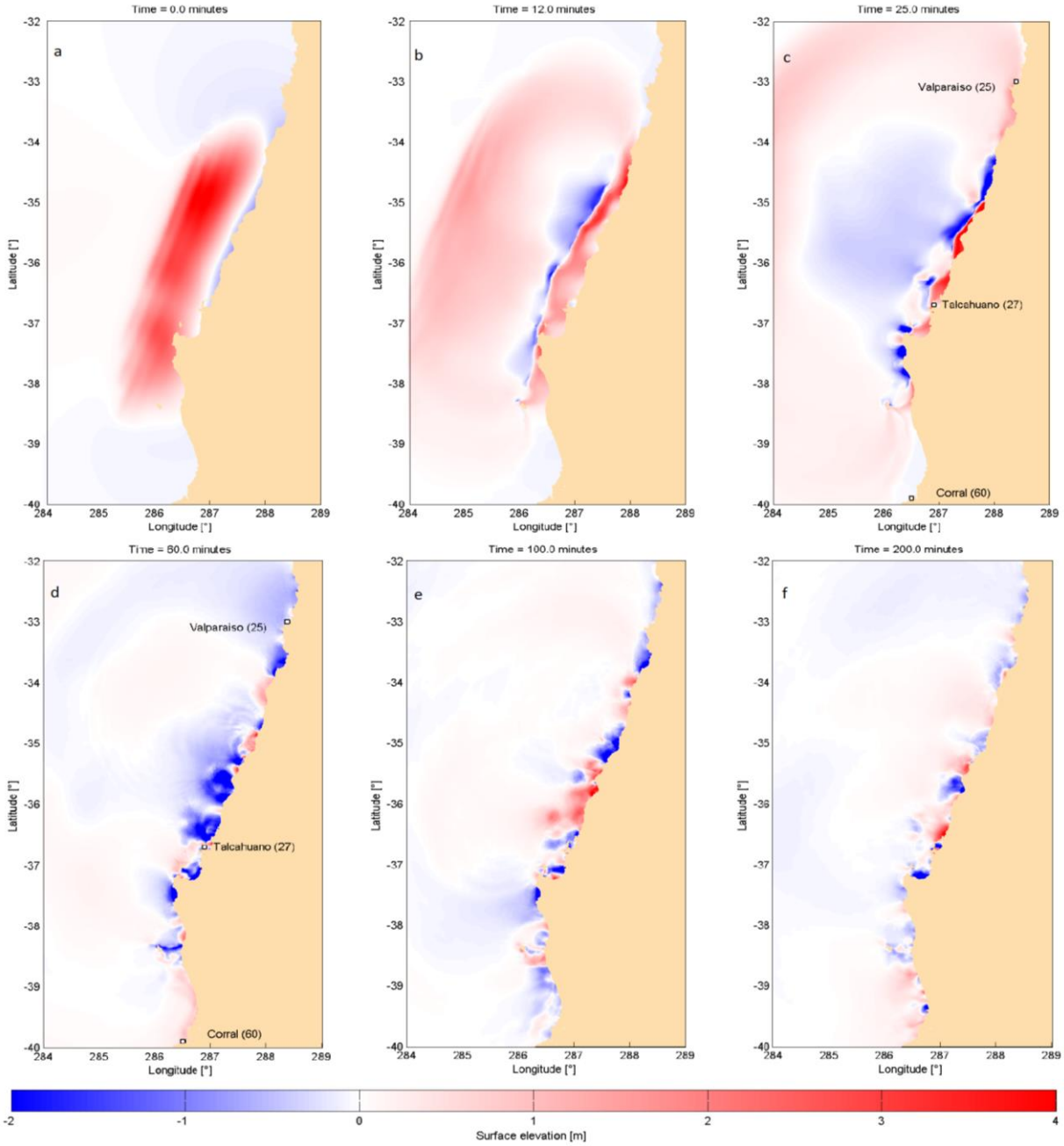

Figure 6.2: Surface elevation at 0, 12, 25, 60, 100 and 200 minutes after initial rupture (Moreno's solution) are visualised in panels a-f respectively. The numbers next to station names (Valparaiso, Talcahuano and Corral) in panels c and d indicate the number of minutes after rupture at which the tsunami was first detected by the tide gauges.

Figure 6.3 shows the surface elevation maps for the Bay of Concepción where the Talcahuano tide gauge is situated. The initial state Figure 6.3-a shows that the tide gauge is located just in the interface between the elevation and subsidence area of the earthquake rupture. Panel b shows the sea surface state after 25 minutes highlighting the arrival of the initial tsunami wave. The offset of 2 minutes between the prediction and observation could be due to the tsunami modelling assumptions and setup, and the sampling rate (2 minutes) of the tide gauge. The last two panels show the surface elevation at 60 and 150 minutes after the rupture. These maps highlight the fact that severe flooding (at 150 min) indeed occurred much later than the arrival of the first and second wave.

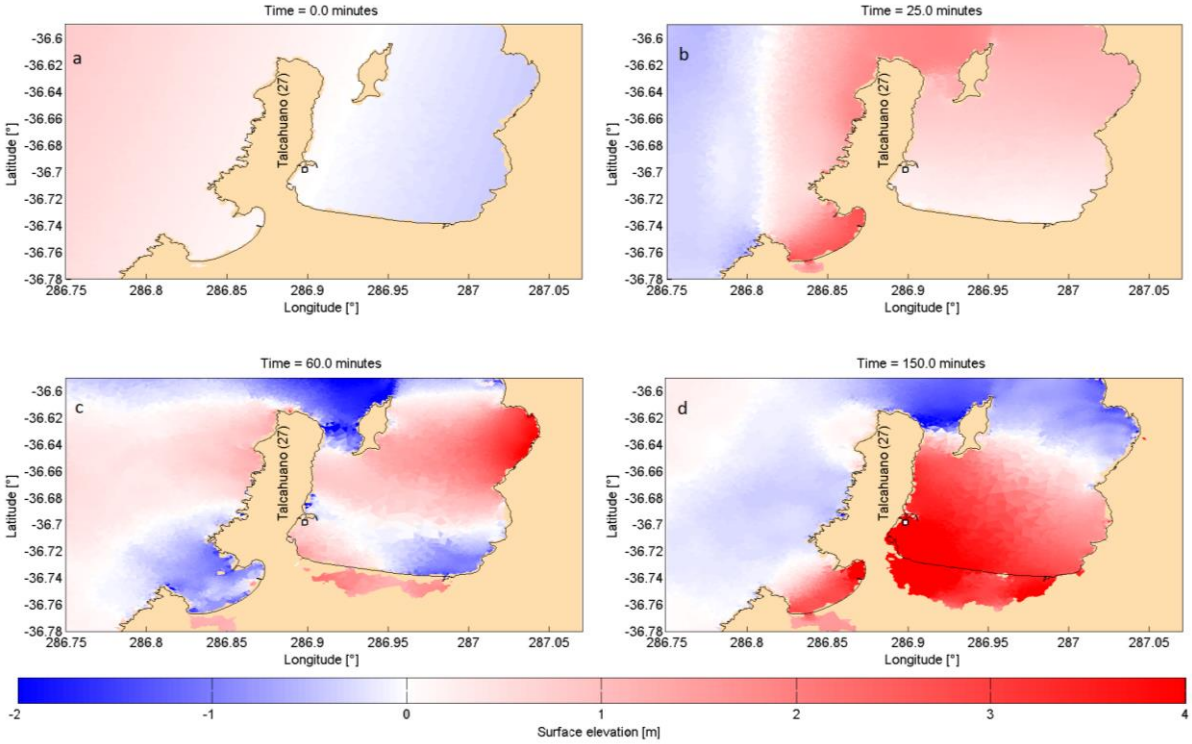

Figure 6.3: Surface elevation at 0, 25, 60, 150 minutes after initial rupture (Moreno's solution). The numbers next to station name indicate the number of minutes after rupture at which the tsunami was first detected by the tide gauges.

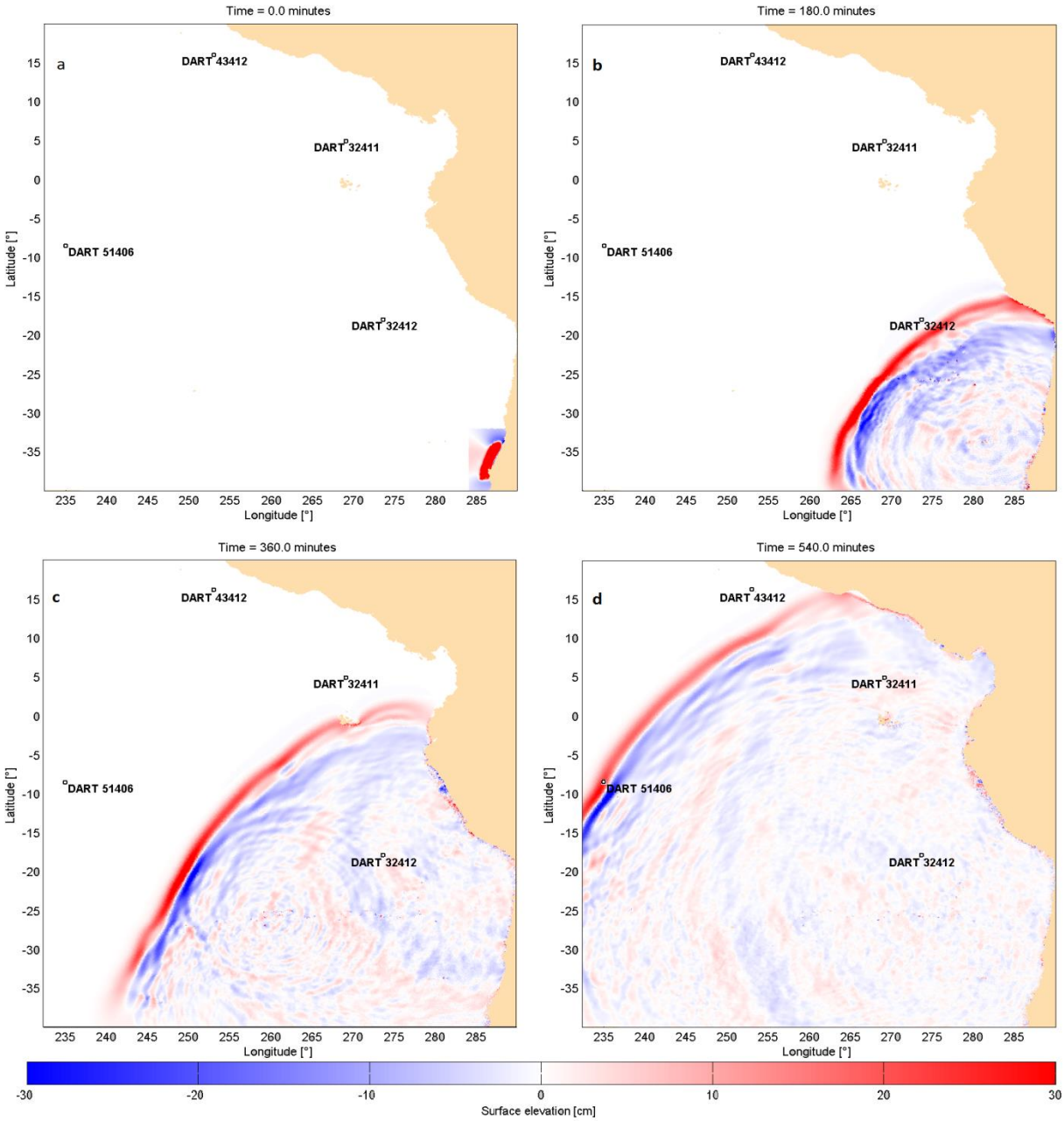

Figure 6.4: Surface elevation at 0, 180, 360 and 540 minutes after initial rupture (Moreno's solution) are visualised in panels a-d respectively.

The surface elevations obtained from the tsunami simulation for the Pacific area is visualised in several maps in Figure 6.4-a shows the initial sea surface using Moreno's solution for the earthquake rupture. Comparing all panels it becomes clear that the tsunami wave indeed travels at a very high speed and that the tsunami retains its energy for thousands of kilometres. In the previous paragraph we stated that the moderate tsunami signal observed at DART 32411 was due to wave refraction and diffraction at the continental margin of the Galápagos Islands. This characteristic is highlighted in Figure 6.4-c. This panel shows that the wave amplitude is much lower around the Galápagos Islands. The reason that the amplitude is relatively high at DART 51406 is highlighted in Figure 6.4-d. It shows that DART 51406 is indeed located in the main energy arc of the tsunami. The circular pattern which is visible in Figure 6.4-b and c is a result of wave reflection at many islands in the South-Pacific Ocean. These reflected waves together with the leaked edge waves, are likely responsible for the persistent wave oscillations in all DART observations as suggested by Yamazaki and Cheung (2011).

6.3. Wave field in frequency domain

In the previous section it is stated that the wave field shows variation in spatial domain in terms of the wave amplitude and dominant wave periods. It is convenient to represent the wave field in the frequency domain to support this presumption more quantitatively. The surface motion time series were transformed to the frequency domain by means of the DFT as explained Chapter 4. The power spectrum, visualised in Figure 6.5, is represented in terms of wave period instead of frequency, because it is simplifies the following discussion.

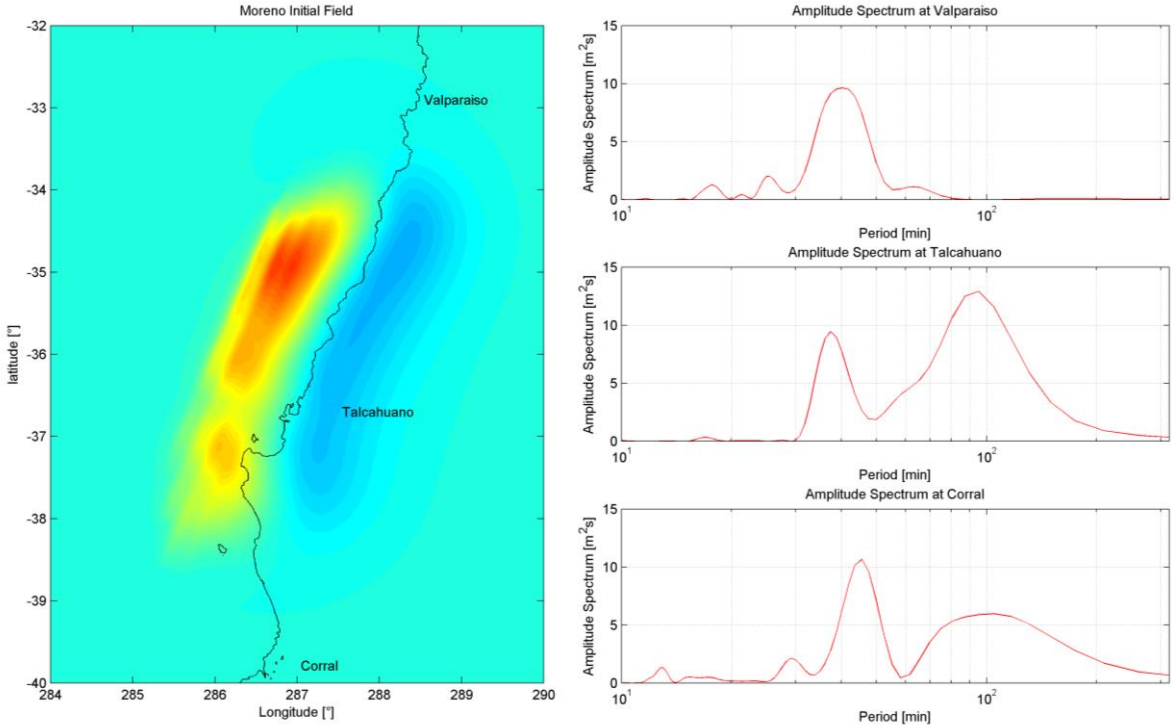

Figure 6.5: (Left) Moreno's initial field and locations of surface elevation output. (Right) Amplitude spectrum, at Valparaiso, Talcahuano and Corral computed with Moreno's initial field as input.

The left panel of Figure 6.5 shows indeed that Valparaiso and Corral are located outside the near-field tsunami region. Starting with the former we clearly see that the peak of the amplitude spectrum occurs at wave periods of 40 minutes. A slight increase in the spectrum is observed at wave periods of approximately 18 and 25 minutes. The wave field at Talcahuano, which is located at the heart of the rupture area, is dominated by longer period waves with a distinct peak at wave period of approximately 93 minutes. The wave field at this location also contains a significant part of its energy in the short period part of the wave spectrum with a peak at a wave period of 35 minutes. It is expected that these relatively short-period waves are generated in the far north from Talcahuano. This expectation will be discussed in more detail with the aid of maps of the energy flux and the surface level at the end of this chapter. The wave field at Corral seems to be characterised by a mixture of the wave spectrum at Talcahuano and Valparaiso. The largest peak occurs at wave period of 45 minutes. A significant portion of the wave energy however is located in the longer-wave period part of the spectrum. The reason for this might be ascribed to the fact that the rupture area is slightly inclined to the south. We suggest that the leaky wave with relative long period measured at Talcahuano migrate further southwards. The property of these waves in contrast to trapped edge waves is that they decay faster in energy (Rabinovich, Stephenson, & Thomson, 2006). This explains why the peak in the amplitude spectrum of Corral at 100 minutes is significantly smaller than the peak amplitude observed at Talcahuano. Rabinovich et al. (2006) stated that the wave field generated by tsunamis in the far field are dominated by trapped edge waves. If we examine the amplitude spectra at Valparaiso and Corral we see that both sites contain a major part of their energy in the relatively short period part of their wave spectrum. We therefore suggest that the

wave energy measured at this band of the wave spectrum might be associated with the presence of edge waves.

6.4. Results of the energy-flux analysis

In this paragraph the results from the energy flux computation will be discussed. The first section will be on the interpretation of the alongshore energy flux. The emphasis in the second section will be shifted towards the cross-shore energy flux. The last section will be on the interpretation of the energy flux maxima.

6.4.1. Alongshore energy flux

The reason for computing the alongshore energy flux is to investigate the role of edge waves in the persistent wave oscillations observed during this tsunami event. The maps of the alongshore energy flux have been visualized in Figure 6.6. Positive energy fluxes in these maps correspond to energy fluxes with a positive direction, i.e. southward direction. The negative signed energy fluxes correspond to northward oriented energy fluxes. The physical interpretation of this quantity is the rate of transfer of energy per unit area. We assumed that the tsunami propagation obeys the 2D SWE. This explain why the computed energy flux represents the rate of energy transfer per unit width.

During wave propagation the waves transport their wave energy along their propagation path. This wave energy transport equals the (wave) energy flux visualized in the following figure. Figure 6.6-a shows the energy flux state at 30 minutes after the earthquake rupture. The second panel shows patches of wave energy flux migrating in southward (red) and northward (dark-blue) direction. Most of the wave energy transportation seems to be confined to the coast which might indicate the presence of coastally trapped edge waves. At the 35^{th} latitude a large part of the wave energy is being transported towards the deep ocean which indicates a leaky edge wave. Panels c and d show that a large patch of wave energy (red circle and arrow) which seems to leak towards the open ocean is refracted back to the coast. This particular wave which appears to be a trapped edge wave propagates further towards the north-facing Bay of Concepción. The arrival of this wave at the Bay of Concepción matches the time at which severe flooding occurred, see Figure 6.3. Another interesting feature depicted by these panels is that all wave energy of this wave seems to be transported into this north facing bay (panel e and f). According to Yamazaki and Cheung (2011) the narrow inlet of this bay resulted into trapping of floodwater and eventually led to severe flooding of the coastal area in the Bay of Concepción (Yamazaki & Cheung, 2011).

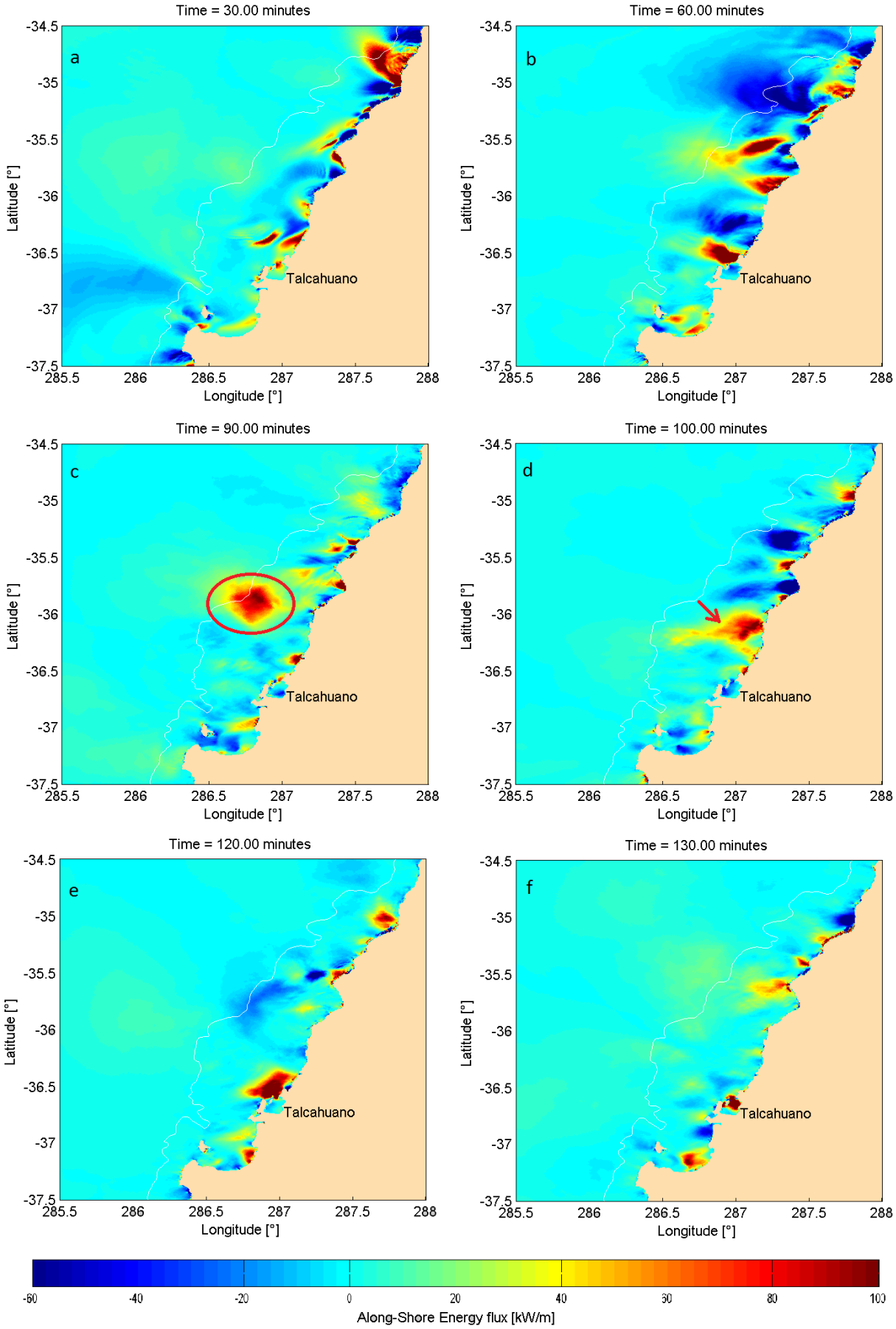

Figure 6.6: Maps of alongshore energy flux at time 30, 60, 90, 100 120, 130 minutes after the earthquake rupture.

6.4.2. Cross-shore energy flux

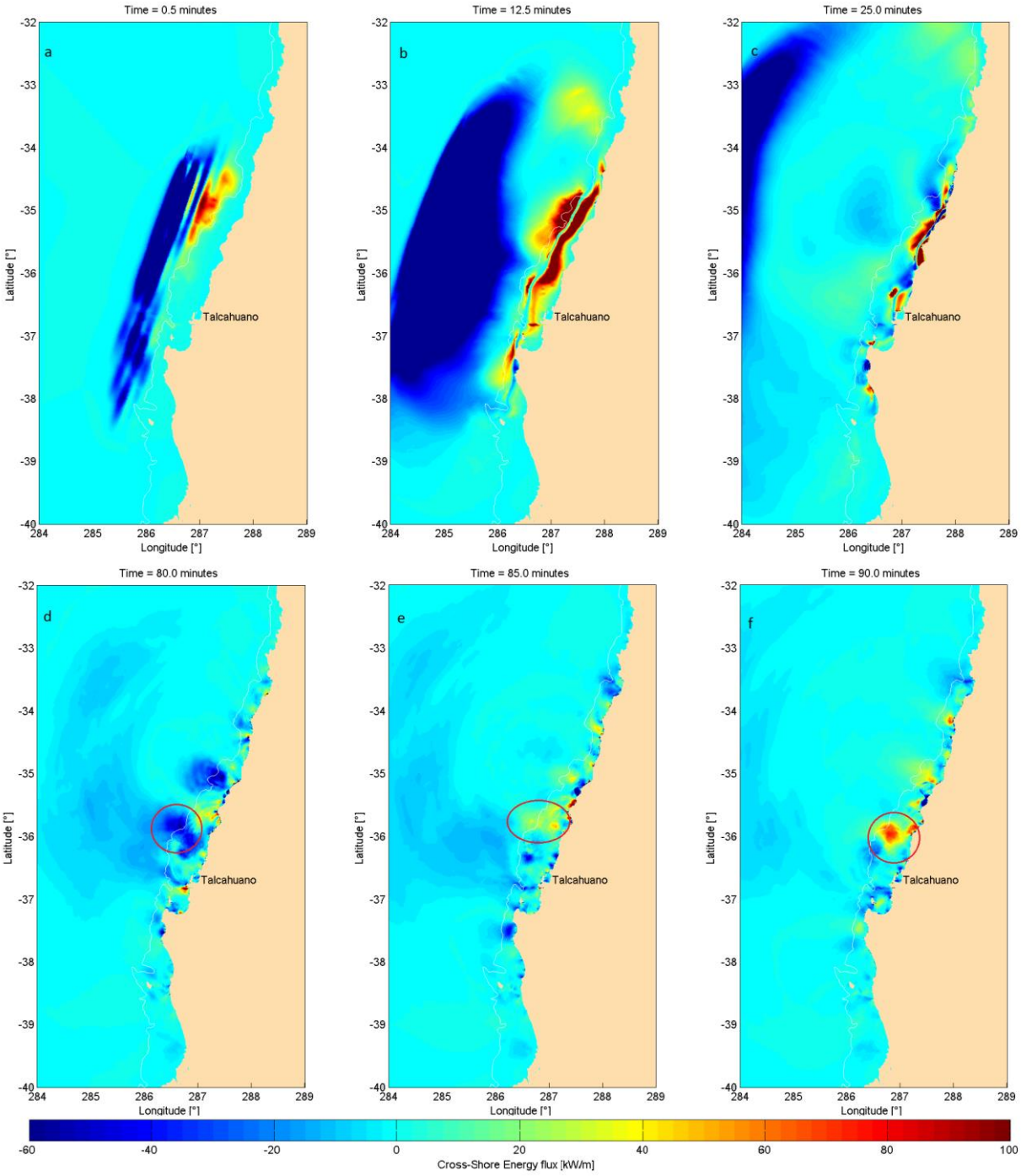

Figure 6.7 Maps of cross-shore energy flux at time 0.5, 12.5, 25, 80, 85, 90 minutes after the earthquake rupture.

Figure 6.7 shows maps of the cross-shore energy flux at several epochs. Positive energy fluxes correspond in these maps with wave energy transported by waves in coastal direction. The reverse holds for negative energy fluxes. The first point that stands out is that only a small portion of the total wave energy is being transported towards the coast. The largest part of the wave energy is headed towards the open ocean highlighted in panels a, b and c. The red circles in these panels highlight the trapping of a wave in coastal region. This is in line with the conclusion of Burgos et al. (2012). They found out by, numerical simulations that the 500 m depth contour is an offshore boundary at which energy is trapped.

6.4.3. Energy flux maxima

The energy flux maxima in cross-shore and alongshore direction are visualized in Figure 6.9 on the next page. The main point of interest of the cross-shore energy flux lies in the portion that is directed towards the coast. We therefore only visualized the (positive) maximum energy flux which is directed towards the shore. The highest energy flux maxima occur at the San Antonio submarine canyons where the bathymetry is characterised by a wide submarine river delta (Figure 6.8). The wide submarine river delta seems to focus the wave energy of the initial tsunami wave through funnelling. It is expected that the funnelling effect of the submarine canyon caused the highest run-up of 29 m at the coastal bluff in Constitución (Fritz, et al., 2010). Panel b and d show that the time of occurrence of the maximum cross-shore and alongshore energy flux respectively. Panel b shows that the cross-shore energy flux in the near field occurs within a few minutes after the initial earthquake rupture. The alongshore energy flux occurs much later in contrast to the cross-shore energy flux. This implies most waves, what appear to be edge waves, are generated after reflection of the tsunami wave at the coast. Furthermore there is a gradual increase in the time at which the maximum occurs outside the near field which implies migration of wave energy along the coast towards the far field.

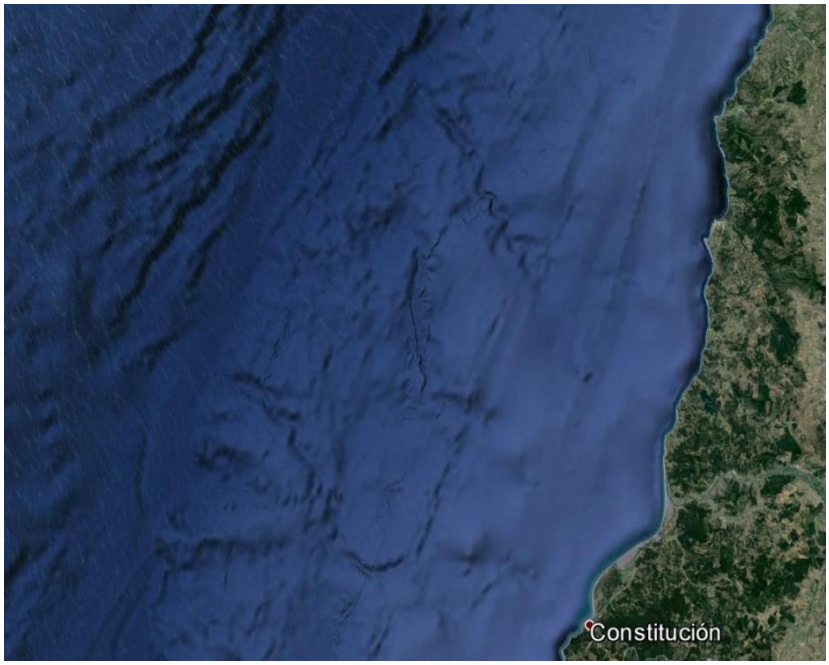

Figure 6.8: Snapshot of the Bathymetry where the highest maximum cross-shore energy flux occurred (Google Earth).

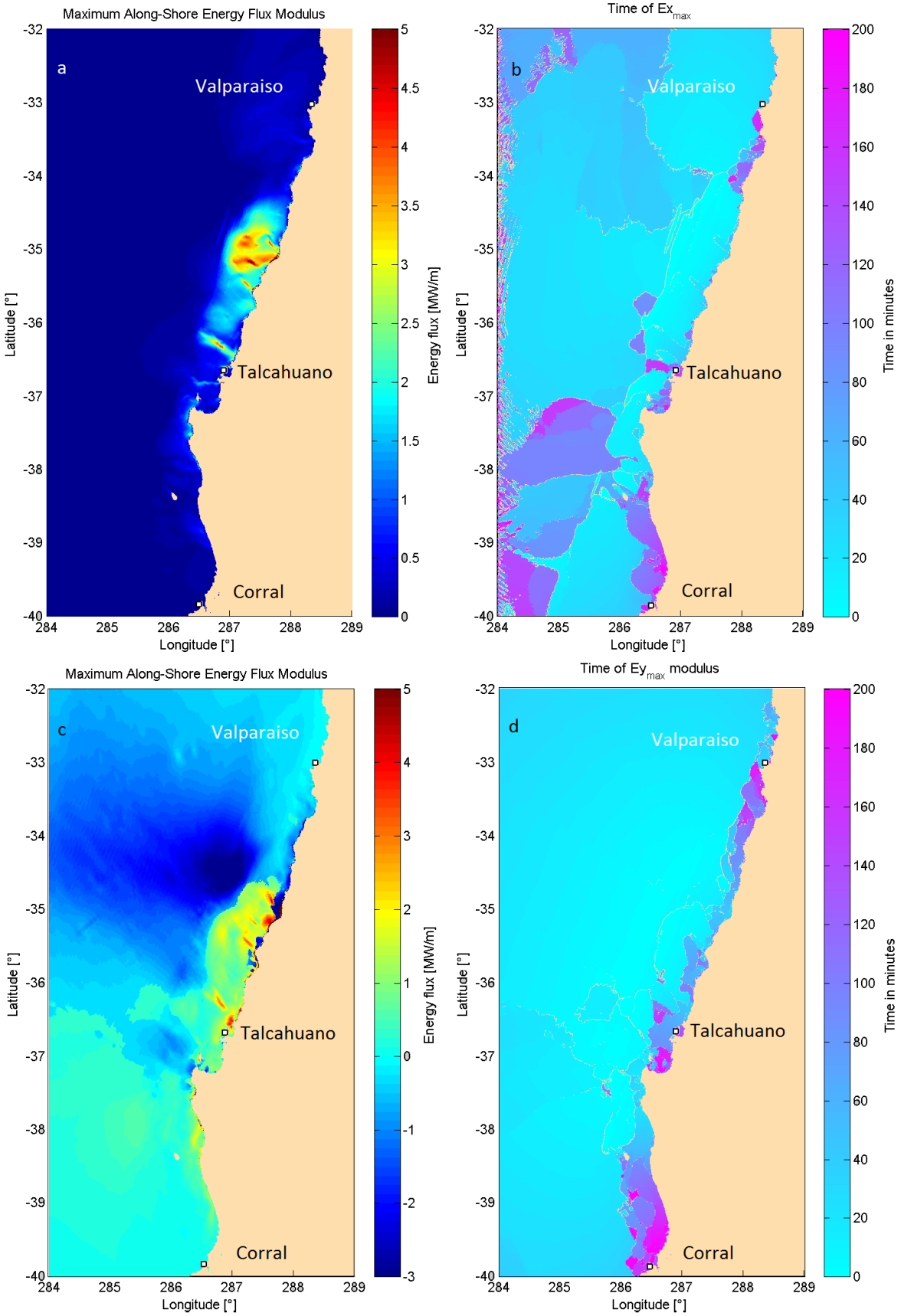

Figure 6.9: Panel a shows the maximum cross-shore energy flux map and panel b shows the time at which the maxima cross-shore energy flux occurs. Panel pair c and d show the maximum alongshore energy flux modulus and the time at which this maxima occurred respectively.

6.5. Role of the Cobquecura submarine canyon

The alongshore energy flux frames visualised in Figure 6.6 suggests that the submarine canyon at the latitude of Cobquecura, 35.8-36^{O}S, (Figure 6.1) plays an important role in the direction of the wave propagation. It is expected that the submarine canyon acts as a wall which reflects and focusses the wave energy towards the shore. The reflection of wave energy is assumed to be a consequence of the large gradient in the depth of the bathymetry. The role of this canyon on the wave propagation will be assessed by simulating the 2010 Chile tsunami with the same initial uplift but using a manipulated bathymetry dataset as input. Panel a of Figure 6.10 shows the actual bathymetry interpolated on the generated mesh with a red square highlighting the canyon of our interest. The canyon has been filled up to compensate for the large depth gradient. The adjusted bathymetry is visualized in panel b in the figure below.

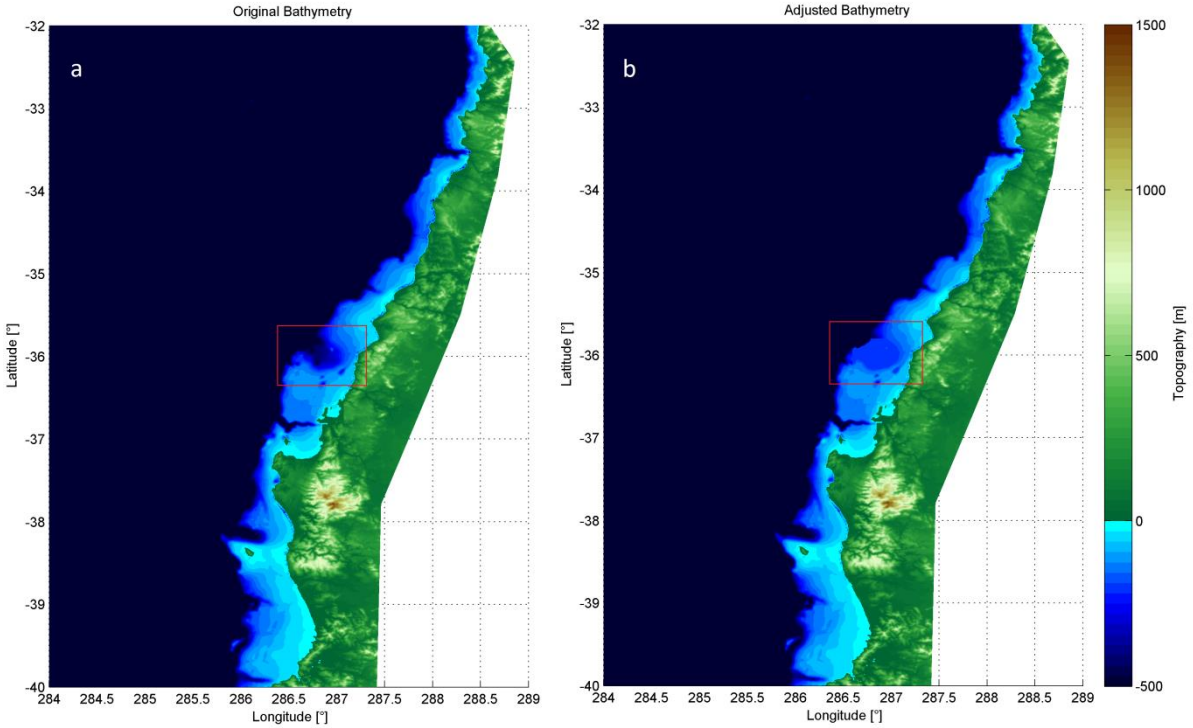

Figure 6.10: Panel a shows the actual bathymetry interpolated on the mesh. Panel b shows the adjusted bathymetry where the submarine canyon has been filled up to a depth of 200 m (red square).

The results of the tsunami simulation using the adjusted bathymetry dataset as input are visualised in Figure 6.11. This figure shows the tsunami impact at Talcahuano harbour for both the real bathymetry (blue line) and the adjusted bathymetry (red line). The results show that the effect of the submarine canyon on the tsunami impact at Talcahuano is rather small. The effect of the submarine canyon is the shift of the surface elevation to the left. The reason for this shift is directly related to filling up the submarine canyon. The wave celerity is proportional with the water depth. So the tsunami waves passing over the flattened submarine canyon will progress slower because of the limited water depth. This results in the slightly delayed arrival of the waves at Talcahuano Harbour. The number of waves and the amplitude of the waves seems to be unaffected by adjusting the bathymetry of the canyon. It can be concluded that this submarine canyon only effects the wave speed of the tsunami waves and has a negligible effect on the wave height i.e. the tsunami impact at Talcahuano Harbour.

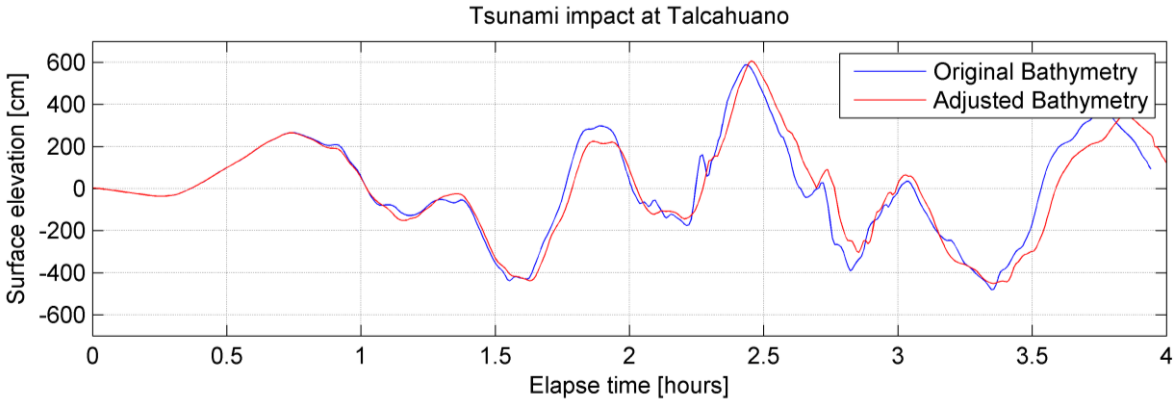

Figure 6.11: Surface elevation time series highlighting the role of the submarine canyon on the tsunami Impact at the Talcahuano harbour.

The effect of the submarine canyon, at the latitude of Cobquecura, on the tsunami wave propagation has been assessed and seems to be negligible. It can be concluded that the small scale bathymetric features, such as submarine canyons discussed here, don't pose an additional effect on the tsunami wave propagation direction as we initially supposed. We suggest that refraction over the continental margin is unaffected by the relatively small submarine canyon discussed here.

6.6. Summary of results

Modelling the 2010 Chilean tsunami using the H_2Ocean unstructured tsunami model resulted in realistic tsunami predictions that fit almost all tsunami signals observed at several DART buoys and tide gauges. The analysis presented here appears to support the findings of Yamazaki and Cheung (2011) that suggest that severe flooding occurred 150 minutes after the initial earthquake shock at the Bay of Concepción is due to edge waves. Figure 6.2 shows what seems to be edge waves trapped along the Chilean coast. In addition the energy flux analysis seems to support the idea that the edge waves are causing this flooding, see Figure 6.6. The wave period computed by means of spectral analysis presented in in Figure 6.5 are consistent with the periods resulting from the analysis carried out by Yamazaki and Cheung (2012).

The Energy flux method presented here shows a wave structure evolution along the coast of Chile which appears to be dominated by the presence of edge waves. However the results and conclusions presented here are somewhat qualitative as a detailed analysis of edge waves is beyond the scope of this research.

7. Discussion

The 2010 Chilean megathrust earthquake generated a destructive tsunami which caused significant damage and loss of life along the coast of Chile, in the Juan Fernández Archipelago and on Easter Island (Fritz, et al., 2010). An intriguing aspect of this event is that the initial wave at Talcahuano harbour was not the largest. A destructive wave arrived approximately three hours after the initial earthquake which caused substantial damage and loss of life. The most sad aspect is that the people who were killed by this wave could have escaped to secure higher ground before the late arrival of this wave. This is in marked contrast to the Indian Ocean Tsunami and The Tohoku Tsunami along the coast of Japan in which the leading tsunami waves caused the greatest flooding, see for example, Pietrzak et al. (2007) and Hooper et al. (2012). Understanding the tsunami response and regions prone to severe inundation and run-up along tsunami prone continental margins is an important area of research.

Several field and numerical studies were conducted to investigate the physics that form the basis of the Chilean Tsunami waves. The paper by Yamazaki and Cheung (2011) on the 2010 Chilean Tsunami is frequently cited in researches on the Chilean Tsunami. Their analysis provides a comprehensive understanding of the wave field observed along the central coast of Chile. With the aid of spectral analysis of the computed surface elevation maps of the spectral energy content and phase angle were derived. These maps show trapping of wave energy along the continental shelf indicating the presence of edge waves. It shows furthermore the natural frequency of several coastal embayment's and the role of the shelf width. The advantage of working in the frequency domain comes at a certain price. The main disadvantage is the loss of the temporal information when transforming the surface elevation time series to compute its spectrum. This leads to the result that their computed spectral energy and phase angle maps are rather static and invariant with time i.e. it only shows the dominant frequencies as function of space. The result of this shortcoming is that they cannot prove their statement that constructive interference of resonance modes of edge waves caused the destructive wave which hit Talcahuano harbour. Another limitation of their research is that they only use the computed surface elevation, a scalar quantity.

We simulated the 2010 Chile tsunami with H_2Ocean unstructured grid tsunami model. The computed surface elevation and velocity time series were processed to compute the energy flux at each epoch. The energy flux quantity uses the computed surface elevation, water depth and the velocity. The directional property of the energy flux allows a separation of the wave field in a cross-shore and alongshore component. Furthermore the energy flux computed at each epoch reveals the signature of edge waves as they propagate over the continental shelf of central Chile. We found with the aid of the energy flux approach that constructive wave interference of two edge waves, over the submarine canyon at the latitude of Cobquecura, forms the basis for the destructive wave which hit Talcahuano harbour three hours after the initial earthquake shock. The energy flux maps show that the wave interference occurred at the shelf edge. This might be the cause of the shelf resonance as discussed by Yamazaki and Cheung (2011).

The energy flux maps revealed that the wave interference occurred over the submarine canyon at Cobquecura. The propagation path of this particular wave, Figure 6.6, suggests that this submarine canyon has a great influence on the wave direction. We assessed the influence this canyon poses on the wave direction by simulating the 2010 Chile tsunami with an adjusted bathymetry dataset as input. The energy flux maps of this simulation were compared to the simulation with the original (real) bathymetry dataset. We additionally checked the tsunami impact in the bay of Concepción for both simulation. The energy flux maps and the surface elevation time series at observation site do

not show any significant difference between the two simulations. The conclusion that can be drawn from these simulations is that the influence of this particular submarine canyon on the wave propagation is negligible and subordinate to wave-refraction. In other words, the small-scale bathymetric features, such as submarine canyons, seem to have no influence on the wave propagation.

Besides the advantages the energy flux method has some limitations. The energy flux method fails to detect the large-scale standing wave systems in the simulation domain. The large-scale standing waves have small amplitudes and they extend far beyond the continental margin (Yamazaki & Cheung, 2011). The energy flux value, which is driven by the surface density of the kinetic and potential energy terms, of the large-scale standing waves is much lower than the energy flux value of progressive (edge) waves. So the combination of their small amplitudes and relatively long wave length makes them undetectable in the energy flux maps. This limitation of the energy flux method implies that we could not quantify the role of the large scale-standing waves on the wave propagation and flooding of the Talcahuano harbour. However we can conclude from the energy flux maps that the role of the large scale standing waves on the tsunami impact at Talcahuano harbour must be subordinate to the role of edge waves. So we can conclude that the tsunami impact observed at Talcahuano harbour must be driven by the trapped wave, what appears to be an edge waves, which are clearly visible in the energy flux maps presented in Chapter 6.

8. Conclusions & recommendations

The main objective of this study was to investigate the 2010 Chile tsunami with the emphasis on the observed resonance oscillations. The 2010 Chile tsunami is modelled with the H_2Ocean tsunami model to gain a better understanding of this event. The conclusions regarding the objectives are presented in this chapter, finally recommendations for further research are proposed.

8.1. Conclusions

What are the capabilities and limitations of H_2Ocean numerical tsunami model in simulating the tsunami?

- The validation test at the tide gauge stations Corral and Valparaiso show a poor fit. The reason for the poor fit at Corral and Valparaiso is not related to the accuracy of the H_2Ocean tsunami model or the chosen model parameters but rather a result of the low resolution of the Bathymetry data.
- In contrast to these stations a much better fit is observed at Talcahuano tide gauge station, which is situated in the region for which a high resolution bathymetry was available.
- The simulation result in the far field show good agreement with the observation in the far field (DART buoys).

The tsunami results generated by H_2Ocean tsunami model show realistic results with all wave characteristic as observed by tsunami recording in both the near and the far field.

What are the effects of the different earthquake scenarios (source models) on the wave field generated at Talcahuano harbour?

- The difference in the generated wave field between the available source model in the far field is negligible.
- Delouis' uplift solution predicts wrong arrival times at the tide gauge stations. Moreno's and Vigny's solution predicts much better tsunami arrival times. These earthquake solutions produce better results because the slip plane is taken closer to the trench.
- Spectral analysis of the computed surface elevations show a small difference in the generated wave field between the different earthquake solutions. This implies that the bathymetry plays an important role in the wave propagation of tsunami waves.

What is the effect of the of the Cobquecura submarine canyon on tsunami propagation?

- The submarine canyon nearby Cobquecura has a negligible effect on the tsunami wave propagation. The small scale bathymetric feature, such as this particular submarine canyons, has a small effect on the tsunami wave propagation. The edge waves are trapped by refraction over gently sloped (wide) continental shelf.

Constructive wave-interference, of an alongshore migrating edge wave with a cross-shore standing wave, is the reason for the destructive wave at Talcahuano harbour three hours after the earthquake

- The energy flux maps show focussing of the wave energy over the Cobquecura submarine canyon. It also highlights a process what seems to be wave interference. However the energy flux method was not able to detect the large scale standing waves. We conclude from this fact that the large scale standing waves are subordinate to the migrating edge waves which are clearly visible in the energy flux maps.

8.2. Recommendations

The following recommendations are proposed for further research on the interaction of tsunami waves with the central coast of Chile:

- The role of bathymetry, shelf width and submarine river canyons on tsunami propagation should be investigated in more details with simulations using uniform bathymetry datasets with varying shelf widths and canyon widths.
- Refraction seems to play a dominant role in the persistent wave oscillation observed during 2010 Chile tsunami. We therefore propose to investigate the role of the initial tsunami wave angle on the tsunami wave trapping and edge wave propagation.
- The connection with the edge wave theory should be done more accurately. Edge wave characteristics should have been estimated using the dispersion relation to prove their presence and importance in the computed wave field.
- Additionally, ray tracing method should be applied to compute the theoretical path of the edge waves over the continental margin due to varying wave speed.

Bibliography

AON Benfield. (2010). *Event Recap Report:02/27/10 Chile Eartquake.* Chicago : Impact Forecasting LLC.

Burgos, L., P., C., & Cienfuegos, R. (2012). Análisis Espectral Aplicado a los Resultados de un Modelo Numérico del Tsunami de 27 de Febrero de 2010 en Chile. *Congreso Latinoamericano de Hidráulica.* San José, Costa Rica.

Centro De Investigación Periodística. (2012, 01 18). Retrieved 11 13, 14, from http://ciperchile.cl/2012/01/18/tsunami-paso-a-paso-los-escandalosos-errores-y-omisiones-del-shoa-y-la-onemi/

Chandrasekera, C., & Cheung, K. (2001). Linear Refraction-Diffreaction Model For Steep Bathymetry. *J. Waterw. Port Coastal Eng.*, 161-170.

Constantin, A., & Johnson, R. (2007). Propagation of very long water waves, with vorticity, over variable depth, with applications to tsunamis. *Elsevier* , 175-211.

Cui, H., Pieterzak, J., & Stelling, G. (2010). A finite folume analogue of the P1^NC-P1 finite element: With accurate flooding and drying . *Ocean Modeling*, 16-30.

Cui, H., Pietrzak, J., & Stelling, G. (2012). *Ocean Modelling*, 55-67.

Delouis, B., Nocquet, J. M., & Vallée, M. . (2010). Slip distribution of the February 27, 2010 Mw= 8.8 Maule earthquake, central Chile, from static and high-rate GPS, InSAR, and broadband teleseismic data. *Geophysical Research Letters*, 37(17).

Encyclopaedia Britanica. (2014). Retrieved from Encyclopaedia Britanica: http://www.britannica.com/EBchecked/topic/1669019/Chile-earthquake-of-2010

Encyclopaedia Britannica Inc. (2006). Retrieved from http://www.britannica.com/EBchecked/topic/437703/Pacific-Ocean

Foreman, M., & Henry, R. (1989). The harmonic analysis of tidal model time series . (12).

Fritz, H. M., Petroff, C. M., Catalán, P. A., Cienfuegos, R., Winckler, P., Kalligeris, N., et al. (2010). Field Survey of 27 February 2010 Chile Tsunami. *Pure and Applied Geophysics*.

GEBCO. (2008). *The General Bathymetric Chart of the Oceans*. Retrieved from http://www.gebco.net

Geist, E. (2013). Near-Field Tsunami Edge Waves and Complex Earthquakes Rupture . *Pure and Applied Geophysics* .

Gonzales, F., Milburn, H., Bernard, E., & Newman, J. (1998). *Deep-ocean Assessment and Reporting of Tsunamis (DART): Brief Overview and Status Report .* Tokyo.

Grinsted, A. (2008, March 7). Retrieved 2014, from http://www.mathworks.com/matlabcentral/fileexchange/19099-tidal-fitting-toolbox

Hanert, E., Le Roux, D., Legat, V., Deleersnijder, E. (2005). An efficient Eulerian finite element method for the shallow water equations. *Elsevier*, 115-136.

Harig, S., Pranowo, W., & Behrens, J. (2008). Tsunami simulation on several scales . *Ocean Dynamics*.

Holthuijsen, L. (2007). *Waves in Oceanic and Coastal Waters.* Cambridge: Cambridge University Press.

Hooper, A., Pieterzak, J. D., Simons, W., Cui, H., Riva, R., Terwisscha van Scheltinga, A., et al. (2012). Importance of horizontal seafloor motion on tsunami height for the 2011 Mw=9.0 Tohoku-Okiearthquake. *Earth and Planetary Science*.

Kowalik, Z., & Murty, T. (1993). *Numerical Modeling of Ocean Dynamics.* World Scientific Publications.
Larrañaga, M. E. (2010). Analisis del Proceso de Toma de Decisiones. *Armada de Chile*.
Mei, C. (1983). The Applied Dynamics of Ocean Surface Waves. *Wiley Interscience*.
Mol, M. (2010). *Modelling the 2010 Chile Tsunami.*
Moreno, M., Rosenau, M., & Oncken, O. (2010). 2010 Maule earthquake slip correlates with pre-seismic locking of Andean subduction zone. *Nature*.
Munger, S., & Cheung, K. F. (2008). Resonance in Hawaii waters from the 2006 Kuril Islands Tsunami. *Geophysical Research*, Letters 35(7).
Munk, W. (1950). Origin and generation of Ocean waves. *Proceedings 1st International Conference on Coastal Engineering*, (pp. 1-4). Long Beach.
National Instruments . (2004). Retrieved from http://zone.ni.com/reference/en-XX/help/370051V-01/cvi/libref/analysisconcepts/aliasing/
NOAA. (1991). Retrieved from http://wcatwc.arh.noaa.gov/?page=tsunami_science
NOAA. (2006, 6 27). Retrieved 11 11, 2014, from http://www.ndbc.noaa.gov/dart/bottom.shtml
NOAA. (2010). Retrieved from NOAA: http://www.srh.noaa.gov/jetstream/tsunami/dart.htm
Pieterzak. (2013). *An Introduction to Oceanography for Civil and Offshore Engineers.* Delft.
Pieterzak, J., Socquet, A., Ham, D., Simons, W., Vigny, C., Labuer, R., et al. (2007). Defining the source region of the Indian Ocean Tsunami from GPS, altimeters, tide gauges and tsunami models. *Earth and Planetary Science letter*, 49-64.
Rabinovich, A., Stephenson, F., & Thomson, R. (2006). The California Tsunami of 15 June 2005 along the Coast of North America. *Atmosphere-Ocean* , 415-427.
Richmond. (2009). Retrieved from http://www.richmond.ca/safety/prepare/city/hazards/tsunamis/tsunamistudy.htm?PageMode=HTML
Roeber, V., Yamazaki, Y., & Cheung, K. F. (2010). Resonance and impact of the 2009 Samoa tsunami around Tutuila,. *Geophisical Research Letters*, 37(21).
Schaefer, J., & Doswell III, C. (1978). *On the Interpolation of a Vector Field.* Kansas City: Monthly Weather Report.
Servicio Sismológico. (2010, April 12). Retrieved October 21, 2014, from Servicio Sismológico: http://www.sismologia.cl/events/sensibles/2010/02/27-0634-28L.S201002.html
Shewchuk, J. (1996). Triangle: engineering a 2D qualitymesh generator and delauni triangulator. *Applied Computational Geometry: Towards Geometric Engineering*.
Teunissen, P., Simons, D., & Tiberius, C. (2009). *Probability and Observation Theory.* Delft: Department of Geoscience and Remote Sensing.
USGS. (2010). *Report on the 2010 Chilean Eartquake and Tsunami Response.* Reston .
Vigny, C., Socquet, A., Peyrat, S., Ruegg, J.-C., Métois, M., Madariaga, R., et al. (2010). The 2010 Mw 8.8 Maule megathrust earthquake of central Chile, monitored by GPS. *Science*, 1417-1421.
Vreugdenhil, C. (1994). *Numerical Methods For Shallow-Water Flow.* Utrecht: Kluwer Academic Publisher.
Webb, D. (1976). A model of continental-shelf resonances. *Deep-Sea Research*.
Willmont, J., Ackelson, S., Davis, R., Feddema, J., Klink, K., Legates, D., et al. (1985). Statistics for the evaluation and comparison of models. *Journal of Geophysical Research* , 8895-9005.
Yamazaki, Y., & Cheung, K. (2011). Shelf resonance and impact of the near-field tsunami generated by the 2010 Chile eartquake. *Geophysical Research Letters*.
Yamazaki, Y., Cheung, K., & Kowalik, Z. (2010). Depth-integrated, non-hydrostatic model with grid nesting for tsunami generation, and run-up. *Int. J. Numer. Meth. Fluids*, 2081-2107.

Appendix A. Energy flux direction

In Chapter 2 a proposition is made to use the energy flux quantity as a tool to identify edge waves in the wave field generated by the tsunami. The main reason for using the energy flux is for its directional properties. In Chapter 2 it was stated that the direction of the energy flux, i.e. the sign of this quantity, is solely based on the sign of the flow velocity vector u or v. In this appendix this statement will be proved algebraically.

$$E_h = \begin{cases} E_x = \rho u h(\frac{1}{2}(u^2 + v^2) + \mathrm{g}\eta) \\ E_y = \rho v h(\frac{1}{2}(u^2 + v^2) + \mathrm{g}\eta) \end{cases} \tag{53}$$

Taking a closer look at the cross shore energy flux E_x it becomes clear that the flux equals the product of two factors: ρuh and $(1/2(u^2 + v^2) + \mathrm{g}\eta)$. The first factor contains the constant ρ which represents the density and the variables h and u which denote the depth and the velocity respectively. The energy flux is calculated only for the wet area which entails that the depth $h \in \Re^+$ does not influence the sign of the energy flux. To prove that the sign of the energy flux only depends on the sign of u the following inequality (or its contrary) has to be verified:

$$\frac{1}{2}(u^2 + v^2) + \mathrm{g}\eta \geq 0 \tag{54}$$

The velocity of long waves is proportional to the water depth $h = d + \eta$, this results in:

$$\begin{aligned} \frac{1}{2}(\sqrt{gh}^2 + \sqrt{\mathrm{g}h}^2) + \mathrm{g}\eta &\geq 0 \\ gh + g\eta &\geq 0 \\ h + \eta &\geq 0 \end{aligned} \tag{55}$$

The depth is a positive real-valued number which is also greater (or equal in the trivial solution) than the wave height η:

$$d + \eta = h \geq \eta \tag{56}$$

This implies that the second factor of the energy flux equation is always positive:

$$\frac{1}{2}(u^2 + v^2) + \mathrm{g}\eta \in \Re^+ \tag{57}$$

This on its turn implies that the energy flux sign is indeed solely determined by the direction of the velocity vector u . Analogously it can be proven that the same holds for the along shore energy flux.

Appendix B. Tidal analysis

Table A.1: Tidal amplitude and phase for tide gauge stations Talcahuano, Corral and Valparaiso estimated by the tidal fitting toolbox. Speed of the tidal constituent equals the frequency which is measured in degrees per solar hour and the Period is in days.

	Amplitude [cm]			Phase [-]			Speed [°/Sh]	Period [day]
	Talcahuano	Corral	Valparaiso	Talcahuano	Corral	Valparaiso		
M2	44,62	41,70	42,60	-2,20	-1,92	-2,43	28,98	0,52
K1	16,60	13,85	13,11	0,53	0,71	1,12	15,04	1,00
O1	11,99	12,42	10,89	3,13	-3,01	3,09	13,94	1,08
N2	9,71	9,98	9,25	2,44	2,73	2,21	28,44	0,53
S2	9,69	9,31	8,97	1,64	1,76	1,35	30,00	0,50
K2	6,35	6,89	6,18	-1,82	-1,79	-2,25	30,08	0,50
R2	6,17	6,42	5,96	1,39	1,33	0,88	30,04	0,50
P1	5,34	3,29	11,89	0,93	1,26	2,27	14,96	1,00
T2	3,55	3,15	6,30	1,96	2,43	2,10	29,96	0,50
MF	3,19	0,76	1,89	2,37	-0,06	1,34	1,10	13,66
MSF	2,47	2,40	3,09	-0,80	2,70	-1,47	1,02	14,77
MU2	2,41	2,62	2,51	-0,46	-0,19	-0,46	27,97	0,54
NU2	2,13	1,75	2,00	1,14	1,77	0,87	28,51	0,53
Q1	2,02	2,20	1,78	1,54	1,88	1,73	13,40	1,12
L2	1,43	1,02	1,16	1,38	1,41	0,79	29,53	0,51
M1	1,37	1,36	1,37	-1,42	-1,19	-1,10	14,50	1,03
J1	1,14	1,07	1,63	2,08	2,08	1,19	15,59	0,96
2N2	0,86	0,72	0,84	0,75	0,88	0,14	27,90	0,54
RHO	0,72	0,21	0,35	0,30	1,20	2,08	13,47	1,11
S1	0,69	4,10	6,89	-1,57	0,46	-0,17	15,00	1,00
OO1	0,67	0,83	1,02	1,75	1,98	2,47	16,14	0,93
MM	0,53	-	0,67	3,14	-	-2,66	0,54	27,55
2Q1	0,38	0,80	0,49	0,41	0,56	-0,28	12,85	1,17
M4	0,27	0,32	0,26	-0,17	2,30	-0,14	57,97	0,26
LAM2	0,20	0,50	0,27	1,74	-2,32	-1,67	29,46	0,51
S6	0,19	0,12	0,17	-1,56	-1,98	-0,64	90,00	0,17
M3	0,16	0,30	0,30	0,19	1,39	-0,48	43,48	0,35
S4	0,14	0,13	0,56	-1,21	-1,87	0,45	60,00	0,25
2SM2	0,12	0,10	0,12	2,61	-0,58	-2,97	31,02	0,48
MK3	0,11	0,65	0,22	-1,20	-1,19	-2,25	44,03	0,34
MN4	0,11	0,11	0,26	-2,67	1,65	3,14	57,42	0,26
2MK3	0,10	0,24	0,04	-1,83	1,13	-2,36	42,93	0,35
M6	0,07	0,14	0,02	-2,08	-1,43	2,78	86,95	0,17
MS4	0,04	0,28	0,04	-2,49	0,51	-3,00	58,98	0,25

M8	0,02	0,01	0,04	2,25	1,88	-0,79	115,94	0,13
Total	135,56	129,75	143,14					